Which global reanalysis dataset represents better in snow cover on the Tibetan Plateau?

Shirui Yan[1], Yang Chen[1], Yaliang Hou[1], Kexin Liu[1], Xuejing Li[1], Yuxuan Xing[1], Dongyou Wu[1], Jiecan Cui[2], Yue Zhou[1], Xin Wang[1, *], Wei Pu[1, *]

[1] Key Laboratory for Semi-Arid Climate Change of the Ministry of Education, College of Atmospheric Sciences, Lanzhou University, Lanzhou 730000, China.

[2] Zhejiang Development & Planning Institute, Hangzhou 310030, China.

Correspondence to: Wei Pu, (puwei@lzu.edu.cn); Xin Wang, (wxin@lzu.edu.cn)

Abstract. The extensive snow cover across the Tibetan Plateau (TP) has a major influence on the climate and water supply for over one billion downstream inhabitants. However, an adequate evaluation of Snow Cover Fraction (SCF) variability over the TP simulated by multiple reanalysis datasets has yet to be undertaken. In this study, we used the Snow Property Inversion from Remote Sensing (SPIReS) SCF data from the Water Years (WYs) 2001–2017 to evaluate the capabilities of eight reanalysis datasets (HMASR, MERRA2, ERA5, ERA5L, JRA55, CFSR, CRAL, and GLDAS) in simulating the spatial and temporal variability of SCF in the TP. The results reveal that HMASR generated the best SCF climatological spatial simulation compared to SPIReS, with the least bias, the highest correlation coefficient, and the highest Taylor Skill Score (SS) value. GLDAS and CFSR also performed well in simulating SCF spatial distribution. In contrast, ERA5L, ERA5, and JRA55 showed relatively good performance in terms of SCF annual trends among eight reanalysis datasets. The biases in SCF simulations across reanalysis datasets are influenced by a combination of meteorological forcings, including snowfall and temperature, as well as the SCF parameterization methods. However, the primary influencing factors vary among the reanalysis datasets. Snow data assimilation could potentially improve SCF simulation accuracy to some extent. Additionally, averaging multiple reanalysis datasets can enhance the spatiotemporal accuracy of SCF simulations, but this enhancement effect does not consistently increase with the number of reanalysis datasets used.

Keywords

Snow cover; Tibetan Plateau; Reanalysis dataset; Meteorological forcing factors; Parameterization methods

1 Introduction

Widespread snow cover on the Tibetan Plateau (TP), with its high albedo and low thermal conductivity, plays a crucial role in the surface energy balance (Zhang, 2005) and affects the climate both locally (Zhang et al., 2022) and across Asia and globally (Lyu et al., 2018; Ma et al., 2017). Furthermore, in its role as the "Asian water tower" (Kitoh and Arakawa, 2016; Qiu, 2008; Xu et al., 2008), the snow that accumulates on the TP during the cold season is an essential freshwater resource for over a billion people during the warm season, supplying their domestic, agricultural, and industrial water needs (Immerzeel et al., 2010). In the context of climate change, the snow cover over the TP is an extremely sensitive element to warming (Yao et al., 2015, 2019; You et al., 2020b). Therefore, the accurate and reliable representation of snow cover over the TP is crucial to regional climate and ecosystem studies.

Ground-based measurements are the most accurate observations with respect to snow cover (Ma et al., 2022). However, the complex terrain and harsh weather conditions on the TP present challenges to comprehensive monitoring (Yang et al., 2019), leading to issues of spatial representativeness. In contrast, optical satellite observations provide global-scale snow cover data and offer crucial support for snow research. For example, NASA's Moderate Resolution Imaging Spectroradiometer (MODIS) has been providing moderate-resolution global daily snow cover fraction (SCF) data since 2000 (Hall et al., 2002). The Snow Property Inversion from Remote Sensing (SPIReS) then uses a more advanced spectral unmixing technique that provides improvements to SCF estimates (Bair et al., 2021). However, the time period covered by satellite and remote sensing data is relatively short, which limits their utility for long-term climate analysis.

Reanalysis methods based on observations and mathematical models (Fujiwara et al., 2017) provide a critical avenue for obtaining long-term snow data. These techniques use data assimilation to integrate historical environmental observations with short-term weather forecasts, yielding optimal estimates of global or regional weather and climate states (Lei et al., 2023). In recent decades, the major meteorological agencies around the world have generated atmospheric and land reanalysis products at varying temporal and spatial resolutions (Fujiwara

et al., 2017). Reanalysis datasets have become indispensable sources of data when it comes to studying processes related to snow variability, as well as their impacts and responses to climate change (Lin and Wu, 2011; Thackeray et al., 2016; Wegmann et al., 2017). For example, the reanalysis snow dataset (e.g., ERA40 and NCEP-NCAR) has revealed that anomalous snow cover in prior autumn facilitates a warm-north, cold-south winter over North America by influencing the teleconnection response in the Pacific-North American (PNA) region (Lin and Wu, 2011). Reanalysis datasets (e.g., MERRA, ERA-Interim, and GLDAS-2) have been integrated into the Canadian Sea Ice and Snow Evolution (CanSISE) dataset to analyze the impacts of global warming on snow changes on the TP (You et al., 2020a).

A comprehensive evaluation of multiple snow reanalysis datasets based on referenced observation data is of paramount importance before launching related scientific research. Previous research has devoted considerable attention to evaluating Snow Depth (SD) and Snow Water Equivalent (SWE) reanalysis datasets using various metrics from different regions (Bian et al., 2019; Li et al., 2022; Wang and Zeng, 2012; Zhang et al., 2021). However, only a few studies have assessed the SCF performance of reanalysis datasets over the TP based on SCF data from the Interactive Multisensor Snow and Ice Mapping System (IMS; Helfrich et al., 2007) and ground observations (Li et al., 2022; Orsolini et al., 2019). These studies have provided comparisons of the SCF spatial patterns among a limited number of reanalysis datasets, and they lack multidimensional analysis that considers aspects such as regional variations and annual trends (Li et al., 2022; Orsolini et al., 2019). In addition, the IMS, which uses microwave remote sensing technology, is challenging for detecting shallow or wet snow that may lead to increased uncertainty in SCF detection (Yu et al., 2013). The discussion by Li et al. (2022) on the simulation errors of SCF in reanalysis datasets appears somewhat lacking. Therefore, prior evaluations of reanalysis SCF datasets are still insufficient.

The various reanalysis snow datasets have unique spatiotemporal characteristics (Mudryk et al., 2015). The differences in snow characteristics originate not only from the use of different Land Surface Models (LSMs), but also from the meteorological forcing data and post-optimization via snow data assimilation. De Rosnay et al. (2014) indicated that the accuracy of

snow simulations is constrained largely by uncertainties associated with some of the key meteorological inputs, including precipitation and temperature (Zhang et al., 2015), under regional climate conditions and elevation factors (Brown and Mote, 2009; Hernández-Henríquez et al., 2015). Therefore, uncertainties associated with precipitation and temperature data are likely to be the primary sources of bias within the reanalysis SCF datasets. Moreover, Jiang et al. (2020) emphasized that optimizing the parameterization methods for SCF calculation would reduce the uncertainties associated with snow modeling, which would further reduce biases in land surface albedo simulations, particularly in high-altitude regions. The reanalysis datasets use different SCF parameterization methods, with a 100% SCF corresponding to an SD that ranges from 2 to 26 cm (Orsolini et al., 2019). The selection of different SCF parameterizations for the reanalysis datasets may lead to varying degrees bias of SCF. On the other hand, data assimilation represents an effective approach to reducing the uncertainties in snow models and enhancing the ability to monitor seasonal snow changes (Andreadis and Lettenmaier, 2006; Sun et al., 2004). Brown et al. (2003) used optimal interpolation (OI) techniques to assimilate SD observations, resulting in gridded monthly SD and SWE datasets that were better aligned with in situ and satellite data across North America.

For this study, we conducted an in-depth evaluation of SCF simulations derived from eight atmospheric and land assimilation reanalysis datasets over the period Water Years (WYs) 2001–2017, using SPIReS SCF data as a reference. The accuracy of SCF was assessed multidimensionally by examining the spatial characteristics, seasonal variations, and annual trends across the whole TP and its nine basins. Additionally, we aimed to assess the influence of meteorological forcing factors (snowfall and temperature), the SCF parameterization methods, and snow assimilation on the SCF biases associated with the various reanalysis datasets. On this basis, we attempted to develop an optimal combination of reanalysis SCF datasets and provide a useful guide for the research community regarding climatic and cryospheric changes over the TP.

2 Data and methods

2.1 Data

2.1.1 Remote sensing data

120   For this study, we utilized the SPIReS SCF data (Bair et al., 2021) as the reference SCF data. It is derived from Landsat 8 Operational Land Imager (OLI) and MODIS data using a spectral unmixing methodology at a 4 km resolution for the period spanning WY 2000 to WY 2021 (e.g., WY 2000 refers to October 1, 1999, to September 30, 2000). The SCF calculation in SPIReS relies on two endmembers (i.e., snow and snow-free) along with an ideal shade component,

125   effectively simplifying the calculation process while maintaining high accuracy. SPIReS reduces the effects of cloud noise through interpolation and smoothing to provide more accurate SCF data (Bair et al., 2021; Dozier et al., 2008). In a comprehensive evaluation conducted by Stillinger et al. (2023) utilizing airborne lidar datasets for subcanopy snow mapping performance over mountain areas in the western United States, spectral unmixing-derived data

130   (including SPIReS and MODIS Snow-Covered Area and Grain Size, abbreviated as MODSCAG) exhibited lower bias and Root Mean Square Error (RMSE) compared to data derived from band ratio methods and spectral mixture methods. Moreover, unlike MODSCAG, SPIReS incorporates the influence of light-absorbing particles on snow, leading to more accurate SCF data.

135   **2.1.2 Reanalysis datasets**

We examined eight widely used reanalysis datasets obtained from various meteorological organizations, with details listed in Table 1. Meteorological forcing fields are used to drive the LSMs, and parameterization methods are used to calculate the daily SCF data. However, the assimilation of snow data varied among the datasets.

140   The High Mountain Asia Snow Reanalysis (HMASR; Liu et al., 2021) is a snowpack-specific reanalysis dataset produced by NASA High Mountain Asia Team (HiMAT). HMASR uses the Simplified Simple Biosphere model, version 3 (SSiB3; Sun and Xue, 2001; Xue et al.,

2003) as the LSM to generate the initial snowpack mass for WYs 2000–2017 based on meteorological inputs from MERRA2 and physiographic characteristics. The model-derived

145 SCF predictions are then constrained by integrating spectral unmixing algorithm derived SCF data from the MODIS and Landsat satellites products (Painter et al., 2009) via data assimilation. The parameterization method used in HMASR (abbreviated as SSiB3_SCF in Table 1) has not been publicly disclosed.

The Modern-Era Retrospective analysis for Research and Applications, version 2

150 (MERRA2; Gelaro et al., 2017) dataset, developed by NASA's Global Modeling and Assimilation Office (GMAO), provides land surface state estimates including SCF via the Catchment LSM (CLSM; Koster et al., 2000). The surface-forced precipitation is a combination of the National Oceanic and Atmospheric Administration (NOAA) Climate Prediction Center (CPC) unified gauge-based analysis of global daily precipitation (CPCU; Xie et al., 2007)

155 product and the precipitation generated by the atmospheric general circulation model within the MERRA2 system. The generated precipitation is also adjusted using a precipitation correction algorithm (Reichle et al., 2017). However, it is important to note that MERRA2 does not include snow data assimilation. The parameterization scheme in MERRA2 considers 100% SCF to occur when the SWE reaches a threshold of 26 kg m^{-2} (abbreviated as MM_SCF in Table 1;

160 Orsolini et al., 2019; Reichle et al., 2017).

The ECMWF Reanalysis version 5 (ERA5; Hersbach et al., 2020), produced and published by the European Centre for Medium-Range Weather Forecasts (ECMWF), uses the Tiled ECMWF Scheme for Surface Exchanges over Land (HTESSEL) model to simulate various land surface variables including SCF. The precipitation forcing in ERA5 is adjusted using

165 Global Precipitation Climatology Project (GPCP; Adler et al., 2003) data. ERA5 assimilates in situ SD observations and binary SCF data from IMS only below 1500 m, so that snow assimilation does not apply to the TP region (Bian et al., 2019). Additionally, a refined dataset known as ERA5-Land (abbreviated as ERAL; Muñoz-Sabater et al., 2021) has been derived from ERA5 via the offline rerunning of the land portion of the model at a higher spatial

170 resolution. ERA5L provides solely land surface parameters and is based on the same forcing

and LSM as ERA5. Both datasets have a 10-cm SD threshold to identify full SCF (abbreviated as ME_SCF in Table 1; ECMWF, 2018; Orsolini et al., 2019).

The Japanese 55-year Reanalysis (JRA55; Kobayashi et al., 2015), developed by the Japan Meteorological Agency (JMA), generates the land surface analysis field using an offline version

175   of the Simple Biosphere (SIB) model (Sato et al., 1989; Sellers et al., 1986). The precipitation forcing is corrected using precipitable water retrieved from the Special Sensor Microwave/Imager (SSM/I) brightness temperature (Onogi et al., 2007). JRA55 incorporates daily SD data from the SSM/I and the Special Sensor Microwave Imager Sounder (SSMIS) using a univariate two-dimensional OI approach. In addition, it assimilates surface synoptic

180   observations (SYNOP) reports and digitizes China's daily SD data from 1971 to 2006 (Onogi et al., 2007). The detection of full SCF in JRA55 is based on a 2-cm SD threshold (abbreviated as MJ_SCF in Table 1; Orsolini et al., 2019).

The Climate Forecast System Reanalysis (CFSR; Saha et al., 2010), developed by the National Center for Environmental Prediction (NCEP) under NOAA, is a weakly coupled

185   global reanalysis system. The land surface analysis utilizes the Noah model (Meng et al., 2012). Two observed global precipitation analyses, namely the CPC Merged Analysis of Precipitation (CMAP; Xie and Arkin, 1997) and the CPCU, are used as alternative forcings for precipitation. In terms of snow analysis, CFSR assimilates IMS and the Global Snow Depth Model (SNODEP). On 1 January 2011, CFSR transitioned to a newer version of the NCEP data

190   assimilation system called CFSv2 (Saha et al., 2014). Despite differences in horizontal resolution and minor changes to the physical parameterization, CFSv2 is considered a continuation of CFSR in most cases (Fujiwara et al., 2017). The SCF parameterization method in CFSR is related to the surface characteristics, using varying SD thresholds to identify the full SCF depending on the underlying surface type (abbreviated as Noah_SCF in Table 1; Ek et al.,

195   2003).

The Global Land Data Assimilation System version 2.1 (GLDAS-2.1; Rodell et al., 2004) is a global land data assimilation product developed jointly by NASA and NOAA. It uses the global meteorological forcing dataset from Princeton University (Sheffield et al., 2006) and the

GPCP V1.3 Daily Analysis precipitation fields (Adler et al., 2003; Huffman et al., 2001) to
drive three distinct LSMs: the CLSM model, the Noah model, and the Variable Infiltration
Capacity (VIC) model. As a result, four datasets are generated (Table S1). Notably, the full
series datasets within GLDAS-2.1 do not assimilate snow observations. Furthermore, owing to
the unavailability of SCF variables in these datasets, this study derived different SCF values
using three parameterization methods (MM_SCF, ME_SCF and MJ_SCF). Finally, the 0.25° ×
0.25° GLDAS–Noah product using the MM_SCF approach was selected as a representative of
GLDAS due to its better SCF simulation (Fig. S1).

China's First Generation Global Atmospheric and Land Reanalysis (CRA-40; Liu et al.,
2023) is produced by the China Meteorological Administration (CMA). The matched land
surface reanalysis datasets (CRA-40/Land, abbreviated as CRAL) are simultaneously generated
offline based on an updated version of the Noah model and atmospheric driving factors from
CRA-40. In CRAL, precipitation meteorological forcing is derived from a similar combination
of data sources as CFSR (Liang et al., 2020). However, CRAL does not assimilate other
observational data in the LSM. Instead, data from over 2,400 CMA surface weather
observatories indirectly influence the land surface product through conventional meteorological
forcing derived from atmospheric reanalysis (Liang et al., 2020). The SCF parameterization
method in CRAL is the same as that in CFSR.

Table 1: Characteristics of the reanalysis datasets used in this study.

Reanalysis dataset	Centre	Temporal coverage	Resolution	Land Model	Snow data assimilation	Variables used in analysis [b]	SCF parameterization method	Reference dataset
HMASR	NASA HIMAT	WY 1999 to WY 2017	1/225°×1/225°	SSiB3	MODIS and Landsat	SCF, SWE, SD	SSiB3_SCF	Liu et al., (2021)
MERRA2	NASA GMAO	1980 to present	0.625°×0.5°	Catchment	-	SCF, SWE, SD, T2, Snowfall	$SCF= min (1, SWE/26)$ [a]	Gelaro et al., (2017)
ERA5	ECMWF	1979 to present	0.25°×0.25°	H-TESSEL	-	SWE, SD, T2, Snowfall, RH	$SCF= min (1, (SD)/10)$ [a]	Hersbach et al., (2020)
ERA5L	ECMWF	1981 to present	0.1°×0.1°	H-TESSEL	-	SCF, SWE, SD, T2, Snowfall	$SCF= min (1, (SD)/10)$ [a]	Muñoz-Sabater et al., (2021)
CRAL	CMA	1979 to present	0.5°×0.5°	Noah	-	SCF, SWE, SD, T2, Snowfall	Noah_SCF	Liu et al., (2023)
JRA55	JMA	1958 to present	0.563°×0.563°	SiB	Station, SSM/I, SSMIS	SWE, SD, T2, Snowfall	$SCF= min (1, (SD)/2)$ [a]	Kobayashi et al., (2015)
CFSR	NOAA NCEP	1979 to present	0.5°×0.5°	Noah	SNODEP, IMS	SCF, SWE, SD, T2, Snowfall	Noah_SCF	Saha et al., (2010); Saha et al., (2014)
GLDAS	NASA and NOAA	2000 to present	0.25°×0.25°	Noah	-	SWE, SD, T2, Snowfall	Noah_SCF	Rodell et al., (2004)

2.1.3 Meteorological dataset

To investigate the effects of snowfall and temperature biases on SCF bias, we used precipitation and 2-m air temperature data from the high-resolution near-surface Meteorological Forcing Dataset for the Third Pole region (TPMFD; Yang et al., 2023) as the reference data. Precipitation and 2-m air temperature in TPMFD were derived by combining a short-term high-resolution Weather Research and Forecasting (WRF) simulation (Zhou et al., 2021), long-term ERA5 data, and in situ observations, all at a resolution of 1/30° for the period spanning 1979 to 2020. Validation conducted by Jiang et al. (2023) demonstrated that the precipitation data from TPMFD are unbiased overall and considerably better than other widely used datasets, including the latest generation of reanalysis (ERA5L), a state-of-the-art satellite-based dataset (the Integrated Multi-satellitE Retrievals for Global Precipitation Measurement, abbreviated as IMERG), and multi-source merged datasets (the Multi-Source Weighted-Ensemble Precipitation version 2, abbreviated as MSWEP v2, and the long-term Asian precipitation dataset, abbreviated as AERA5-Asia). To obtain snowfall data for our study, we applied a dynamic threshold parameterization scheme, which considers surface air conditions such as wet bulb temperature, surface elevation, and relative humidity, to convert precipitation data in TPMFD to snowfall. This approach has been proven effective in capturing snowfall variations on the TP through comparisons with station observations (Ding et al., 2014) and has been used in many studies (Deng et al., 2017; Luo et al., 2020; Yang et al., 2021; Zhu et al., 2021). For detailed calculation methods and further information, readers are referred to the work of Ding et al. (2014). We note that TPMFD lacks the relative humidity variable necessary for snowfall conversion, while all variables in TPMFD are assimilated from ERA5 data. Therefore, we utilized ERA5 surface relative humidity as a substitute.

2.2 Study region

The boundary of the TP used in this study is identified as an isoline of 2,500 m according to the Global Multi-resolution Terrain Elevation Data 2010 (Danielson and Gesch, 2011), spanning from 26°N to 41°N and from 67°E to 105°E (Fig. 1b). The prevailing westerlies and monsoons are the primary moisture sources in this region, exerting significant influence on the spatial and temporal distribution of snowfall and glacier mass balance (Liu et al., 2021; Yao et al., 2012). Specifically, the westerlies dominate winter precipitation, while the Indian and East Asian monsoons dominate summer precipitation in the southeast (Yao et al., 2012), resulting in diverse snow regimes. We identified nine major river basins within the TP using Hydrological Data and Maps Based on Shuttle Elevation Derivatives at Multiple Scales (HydroSHEDS; Lehner et al., 2008), namely the Amu, Indus, Tarim, Inner Tibetan Plateau (abbreviated as ITP), Brahmaputra, Salween, Mekong, Yangtze, and Yellow basins. Due to the differing impacts of winter and summer atmospheric forcing, the performance of SCF simulations from reanalysis datasets varies across these basins.

2.3 Methods

2.3.1 Evaluation of SCF accuracy for reanalysis datasets

In this study, we used time series spanning from WYs 2001–2017, covering periods for which all data were available. Before our evaluation, all data were regridded via the bilinear interpolation method to 0.5°×0.5° grids, ensuring the resolution uniformity between different datasets. After unifying the resolution, all datasets included 1200 pixel points in the TP.

We employed absolute bias and Pearson's correlation coefficient (R) as the evaluation metrics for assessing SCF accuracy. To visually capture the spatial variability of SCF climatology across multiple dimensions in the reanalysis datasets, Taylor diagrams (Taylor, 2001) were further employed to represent the combined information of R, RMSE, and Standard Deviation Ratio (STDR). These three metrics in the Taylor diagrams of Fig. 2b were computed for 1200 pixel points within the TP between reanalysis datasets and SPIReS after averaging the

SCF climatology from WY 2001 to WY 2017. R and RMSE describe the degree of phase and amplitude agreement of the reanalysis SCF climatological spatial fields with SPIReS. To facilitate comparison across reanalysis datasets in one Taylor diagram, we normalized the Standard Deviation (STD) to obtain STDR, representing the consistency in dispersion of spatial field values between reanalysis datasets and SPIReS (Cui et al., 2021). Better performance is indicated by relatively higher R, lower RMSE, and closer STD (in other words, STDR closer to 1). Additionally, Taylor Skill Scores (SS, ranging from 0 to 1; Taylor, 2001) were calculated to provide comprehensive statistics for the composite index. The SS is defined as follows:

$$SS = \frac{4(1+R)^4}{(STDR + 1/STDR)^2 (1+R_0)^4} \tag{1}$$

where R_0 is the maximum correlation attainable. The R and RMSE required to calculate SS in Fig. 4 are consistent with the method described above, but for different seasonal averages for SCF climatology.

The reliability of annual trend analysis depends on the significance testing, and the sign ($+$ or $-$) may impact the robustness of the annual trend analysis results. Therefore, we used the Mann-Kendall (MK; Kendall, 1975; Mann, 1945) test to ascertain the significance of annual trends, and the Consistency Index (CI; Zhang et al., 2021) to validate the SCF annual trends. The CI is defined as follows:

$$CI = \frac{N_{inc} + N_{dec} + N_{no}}{N_{tot}} \tag{2}$$

where N_{inc} is the number of grid points with a significant increasing trend in both the reanalysis dataset and SPIReS ($P < 0.05$), N_{dec} is the number of grid points with a significant decreasing trend in both datasets, N_{no} is the number of grid points with a non-significant trend in both datasets, and N_{tot} is the total number of grid points. The higher the CI value, the better the performance of the trend simulation.

2.3.2 Analysis of SCF bias sources and generation of optimal datasets

Variations in snowfall and temperature are the dominant influences on snow evolution and can explain half to two-thirds of the interannual variability in snow cover (Xu et al., 2017). Hence, biases in snowfall and temperature within reanalysis datasets are likely the main sources of bias

in SCF. Here, the analysis of bias sources was primarily based on correlation analysis between the bias of SCF and those of snowfall and temperature. Similar to the SCF case, the absolute biases of snowfall and temperature were computed by comparing the reanalysis datasets with TPMFD. Additionally, we calculated the R between the time series of annual average biases in snowfall and temperature at each pixel point over the TP and SCF biases to obtain the spatial distribution of correlations as shown in Fig. 3.

In the snow model, optimizing the SCF parameterization method can significantly reduce the annual SCF biases (Jiang et al., 2020). For the eight reanalysis datasets here, five parameterization methods were used to convert SWE or SD into SCF; i.e., MM_SCF, ME_SCF, MJ_SCF, SSiB3_SCF, and Noah_SCF (see Section 2.1.2 and Table 1). These parameterization methods have been evaluated in diverse regions (Orsolini et al., 2019), and the results indicate that different parameterizations of snow processes will introduce different uncertainties into snow simulations (Jiang et al., 2020). Moreover, specific challenges arise on the TP because of its complex terrain and unstable snow conditions (Huang et al., 2023). In order to evaluate the impact of the parameterization method on SCF simulations, we incorporated three publicly available and easily offline-usable parameterization methods (MM_SCF, ME_SCF, and MJ_SCF) separately into each reanalysis dataset to derive another three (two) SCF products for HMASR, CRAL, and CFSR (MERRA2, ERA5, ERA5L, JRA55, and GLDAS).

Mortimer et al. (2020) demonstrated that product accuracy can be enhanced by averaging multiple reanalysis datasets, as this allows unrelated errors and deficiencies between them to offset each other. To investigate whether averaging of multiple datasets can improve SCF accuracy over the complex terrain of the TP, we considered all possible combinations of the eight reanalysis datasets, totaling 247. The output of each combined dataset was computed as the equally weighted average of all reanalysis datasets in the combination (Mudryk et al., 2015). Subsequently, we characterized the SCF accuracy of combined datasets in spatial distribution and annual trends by computing the SS and CI values.

3. Results

3.1 Spatial variability of SCF climatology

3.1.1 Evaluation of spatial variability

The reanalysis datasets exhibit a range of SCF patterns over the TP (Fig. 1a). The basin-averaged values were obtained by averaging pixel points within each basin of the TP after SCF climatological average from WY 2001 to WY 2017 (Fig. 1b). The TP average of SCF climatology from HMASR, GLDAS, and CRAL are 0.14, 0.12, and 0.12, respectively, which align closely with the SPIReS value of 0.13. In more detail, HMASR (GLDAS and CRAL) displays a slight underestimation (overestimation) in westerlies-dominated basins such as the Amu and Indus, and overestimation (underestimation) in monsoon-dominated basins such as the Yellow, Yangtze, Mekong, Salween, and Brahmaputra (Fig. 2a). These biases probably average out when looking at the TP as a whole, resulting in more accurate reanalysis SCF simulations. On the other hand, ERA5, ERA5L, and JRA55 show large positive SCF biases across all basins, whereas MERRA2 displays a large negative bias in SCF. In comparison to SPIReS, ERA5 stands out as the dataset showing the highest positive bias, while MERRA2 demonstrates the largest negative bias, with extreme TP average values of 0.41 and 0.05, respectively (Fig. 1b).

Figures 1a and 2a further show that, although all reanalysis datasets have spatial SCF patterns that are similar to those from SPIReS, the varying magnitude of SCF value across these datasets results in different correlations (characterized by R values), bias (characterized by RMSE values) and similarities in dispersion patterns (characterized by STDR values) when compared with SPIReS, which ultimately influences their synthesis performance (characterized by SS values). In the Taylor diagram (Fig. 2b; see Fig. S2 for a clearer version), HMASR has the highest R values across all basins, with STDR values for monsoon-dominated basins close to 1 (e.g., 1.01 for the Salween basin). Consequently, HMASR achieves the highest SS value of 0.68, indicating its superior SCF spatial performance across the TP. Following HMASR, GLDAS comes next, with its R values ranking second in the TP. Meanwhile, GLDAS captures

high SCF climatological values in the Tarim and Indus basins and low values in the ITP, Yellow, and central Brahmaputra basins, similar to SPIReS (Fig. 1a), giving it better STDR values in the TP compared to HMASR (Fig. 2b). CFSR consistently exhibits high R values across all basins, despite its positive bias in the TP average of SCF climatology. Consequently, CFSR has an SS value of 0.57, similar to GLDAS. In contrast to CFSR, although CRAL has a TP average close to SPIReS, its spatial distribution is overly uniform, with a relatively low R value and high RMSE, leading to a moderate SS value. Other reanalysis datasets that overestimate SCF climatology, such as ERA5, ERA5L, and JRA55, are able to capture STDR well in some basins, but their large biases result in high RMSE and low SS values in the TP, consistent with Bian et al. (2019). MERRA2 shows the worst STDR and SS value, not only across the TP but also within each basin. This seems opposite to the conclusions of Orsolini et al. (2019), who found MERRA2 to perform well in capturing the SCF and SWE characteristics on the TP. The reason for this discrepancy is that their results depended mainly on the high correlation between MERRA2 and the reference dataset, while overlooking the severe underestimations in SCF values. These underestimations result in a very small self-STD in the STDR calculation, leading to the worst SS value in this study of 0.16.
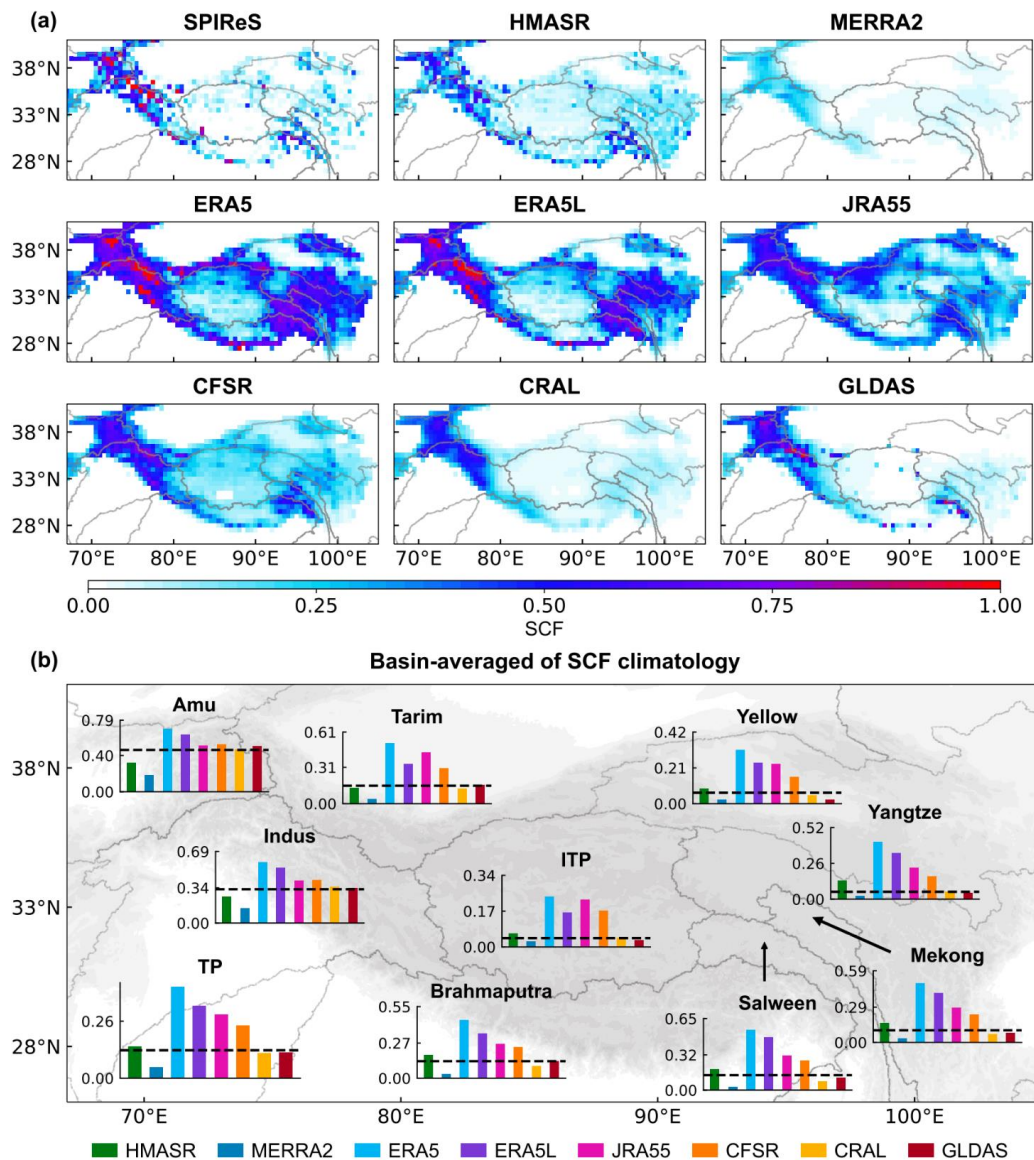
Figure 1: (a) Spatial distribution of Snow Cover Fraction (SCF) climatological average for Water Years (WYs) 2001–2017 from SPIReS and eight reanalysis datasets over the Tibetan Plateau region. (b) Basin-averaged of SCF climatology from SPIReS (black horizontal line) and the eight reanalysis datasets overlain on a map of the TP. ITP = Inner Tibetan Plateau.

For each reanalysis dataset, the SCF simulation exhibits varying spatial performance over different TP basins, influenced by their unique topographic and climatic characteristics. Basins affected primarily by the winter westerlies (e.g., the Amu and Indus basins) display better consistency between reanalysis datasets and SPIReS. The Indus basin shows the best SCF spatial performance with the highest SS value (Fig. 2c). In basins influenced by the summer monsoon (e.g., the Yellow, Yangtze, Mekong, Salween, and Brahmaputra basins), SCF spatial performance varies. The basin-averaged of SCF climatology is highly biased in the Yellow and

380   Yangtze basins for the reanalysis datasets (Fig. 1b). Specifically, the SCF climatological basin-averaged values of ERA5, ERA5L, and JRA55 (MERRA2) are more than 2× larger (lower) than SPIReS. These biases result in varied RMSE and STDR among these reanalysis datasets (Fig. 2b) and lower SS values (Fig. 2c). However, this phenomenon is less pronounced in the Salween and Brahmaputra basins, where SS values are relatively higher. The Tarim and ITP

385   basins are considered inland basins. In particular, the ITP basin shows the poorest SCF spatial performance among basins, with the SS values of the reanalysis datasets <0.15, except for HMASR.
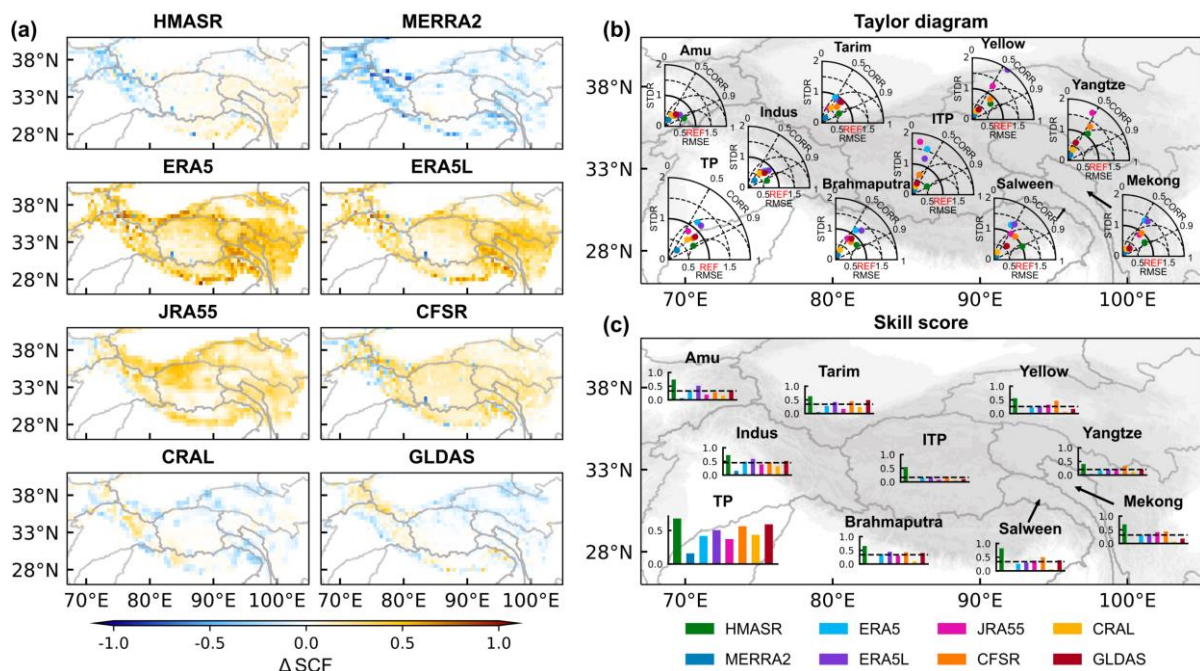
Figure 2: (a) Spatial distribution of the SCF climatological bias from the reanalysis
390   **datasets based on SPIReS over the TP. (b) Taylor diagrams showing the correlation coefficients (R), Root Mean Square Error (RMSE), and Standard Deviation Ratio (STDR) of SCF between reanalysis datasets and SPIReS for each basin, overlain on a map of the TP. (c) Taylor Skill Scores (SS) for each basin overlain on a map of the TP. The black line is the average of the SS values for all reanalysis datasets in basin.**

395   **3.1.2 Bias attribution in the spatial distribution of SCF**

The evolution of SCF can be determined from the balance between snow mass gain via snowfall and snow depletion via snowmelt, sublimation, and wind drifting (Liu et al., 2022), while snowfall and snowmelt are strongly dependent on temperature (Serquet et al., 2011; Vorkauf et al., 2021). Hence, the accuracy of these two pivotal meteorological forcing factors, snowfall

400 and temperature, directly impacts the integrity of the LSMs (Zhang et al., 2015). In addition, different SCF parameterizations influence the instability inherent in the snow models (Dutra et al., 2011; Jiang et al., 2020), and the data assimilation techniques also affect the final results of SCF simulations (Magnusson et al., 2017). Therefore, we further investigated the SCF bias by examining the performance with respect to snowfall and temperature in each reanalysis dataset,

405 along with the inadequacies of parameterization methods. Moreover, by discussing snow data assimilation among reanalysis datasets, we tried to understand its impact on SCF accuracy.

ERA5, ERA5L, and CFSR overestimated snowfall in both the westerlies-dominated and monsoon-dominated basins (Fig. 3, first column on left). The snowfall biases are particularly pronounced in the western and southeastern regions of the TP, including on the Pamir Plateau

410 and the southern slopes of Mount Namcha Barwa. The only exception is the inland basin of the ITP, where snowfall is underestimated. In contrast to snowfall, these reanalysis datasets consistently underestimated temperatures in westerlies-dominated and monsoon-dominated basins (Fig. 3, third column on left). The excessive snowfall contributes to heightened snow accumulation, while the reduced temperatures hinder the ablation process by impeding the snow

415 from attaining the freezing threshold (Liu et al., 2022). Simultaneously, under conditions of adequate atmospheric water vapor, low temperatures further intensify snow accumulation through enhanced snowfall (You et al., 2020b). The combined impacts result in a positive SCF bias within ERA5, ERA5L, and CFSR, characterized by significant correlations between snowfall and temperature bias versus SCF bias. Moreover, compared with snowfall,

420 temperature bias exhibits stronger significant correlations with SCF bias over broader areas. This implies that physical processes influenced by temperature bias may have a more pronounced and widespread responsibility with respect to SCF bias.

For MERRA2, CRAL and GLDAS, the SCF climatology shows large biases in the westerlies-dominated basins, as well as in the Tarim and Brahmaputra basins, where a

425 significant correlation exists between snowfall and temperature biases and SCF bias. This suggests that both snowfall and temperature play equally important roles in influencing the SCF biases in MERRA2, CRAL and GLDAS.
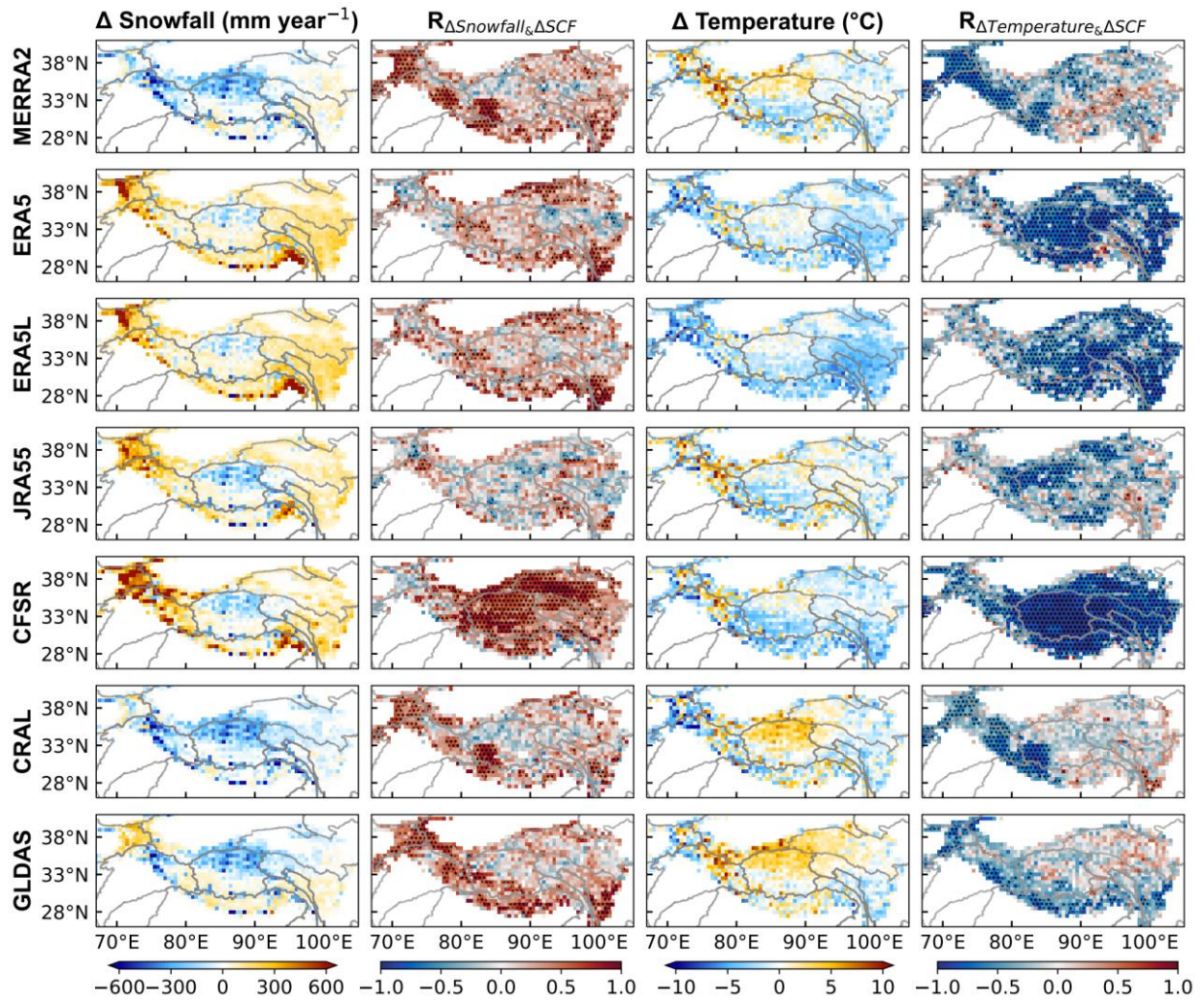
Figure 3: The columns show (from left to right): spatial distribution of the snowfall climatological bias for the reanalysis datasets based on TPMFD over the TP; spatial distribution of the R value between snowfall bias and SCF bias; spatial distribution of the temperature climatological bias for the reanalysis datasets based on TPMFD over the TP; and spatial distribution of R values between temperature bias and SCF bias. Black dots in the second and fourth columns indicate that the correlation exceeds the 95% confidence level. HMASR and MERRA2 share the same meteorological forcing data.

JRA55 shows similar patterns and magnitudes of snowfall and temperature biases to ERA5, ERA5L, and CFSR, but these two meteorological factors can explain SCF bias in only limited areas. In addition, Orsolini et al. (2019) found that JRA55 performs well in SD simulation due to assimilating SD data from ground observation stations in China. Thus, the conversion process from SD to SCF within LSM in JRA55 may affect the accuracy of SCF simulations. Indeed, JRA55 uses an aggressive parameterization approach with a 2-cm SD threshold to define the complete SCF, which differs markedly from other reanalysis datasets (see Section 2.1.2 and

Table 1). When adopting a more appropriate parameterization method (see Fig. 9), the SCF simulation by JRA55 shows a noteworthy increase in the SS value from 0.37 to 0.5. This apparent improvement confirms the importance of the parameterization method to SCF accuracy in JRA55.

An interesting observation is that while MERRA2 and HMASR share the same meteorological forcing data but differ in snow assimilation situation. HMASR directly assimilates SCF data obtained from MODIS and Landsat satellites (Liu et al., 2021), which are processed using a spectral unmixing algorithm that has been found more accurate than the original band ratio methods (Stillinger et al., 2023). Therefore, the assimilation of high-precision satellite SCF data enhances the SCF simulation in HMASR, while the lowest SS value obtained by MERRA2 in SCF spatial simulations was likely related to its lack of SCF data assimilation. As for JRA55 and CFSR, which although assimilated SD data and have been found good simulations in SD and SWE (Bian et al., 2019; Orsolini et al., 2019), the process of transforming SD to SCF through model parameterization introduced additional errors, thereby leading SD assimilation to only a limited effect on the accuracy of SCF simulations. Compared to JRA55, the SCF parameterization method employed in CFSR is more reasonable, resulting in spatial simulation performance batter than JRA55 by a considerable margin. This indirectly illustrates the impact of parameterization methods on the SCF simulation in JRA55.

3.2 Seasonal evolution and annual trends in SCF

3.2.1 Evaluation of seasonal evolution and bias attribution

Figure 4 shows the SCF bias, its probability density distribution, and the SS values for the four seasons. In general, the different seasons show similar spatial patterns of SCF bias for each reanalysis dataset, which is consistent with the climatological SCF bias results (Fig. 2a). This suggests the persistent influence of the uncertainties associated with the snowfall and temperature data, on the SCF bias throughout the year. However, the bias values vary seasonally (Fig. 4), with higher biases observed during the accumulation period (winter and spring), but lower biases during the ablation period (summer and autumn). The largest bias in winter can be

several times larger than the lowest bias in summer. However, this does not imply a better SCF simulation for summer than winter. As the SCF during winter is much higher than that during summer (Fig. S3), a smaller fractional difference in winter can result in a larger absolute bias. Conversely, higher R values and better STDR values (in other words, STDR closer to 1) in seasonal SCF between the reanalysis datasets and SPIReS are obtained during the accumulation period than the ablation period (Table S2), leading to a better SCF spatial performance for winter and spring, as shown by the larger SS values (Fig. 4). The seasonal variability associated with the SCF simulation performance is most evident in MERRA2 and CRAL.
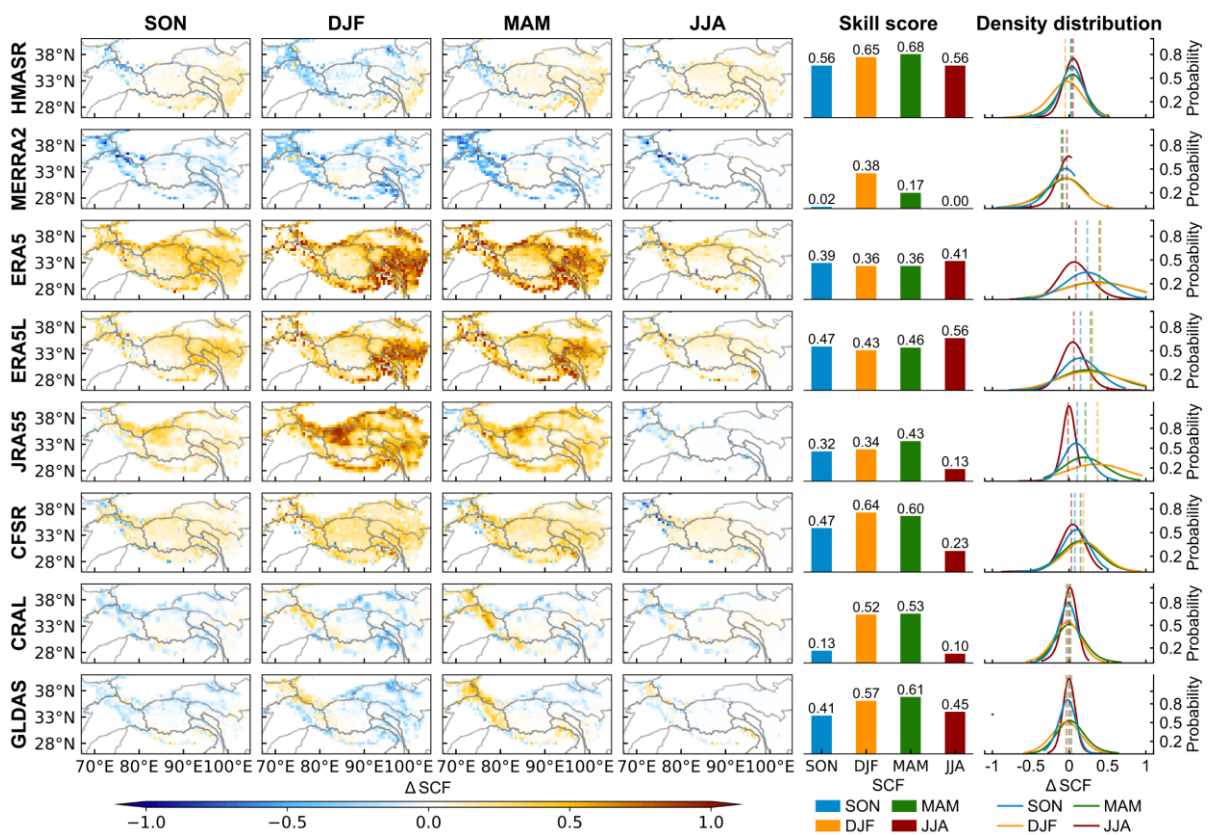
Figure 4: The first four columns show the spatial distribution of seasonal SCF climatological bias from the reanalysis datasets based on SPIReS over the TP during (left to right): autumn (September–November: SON), winter (December–February: DJF), spring (March–May: MAM), and summer (June–August: JJA). The SS values of seasonal SCF climatology are shown in the fifth column. The probability density distribution of seasonal SCF climatological bias is shown in the sixth column. The dashed lines in the sixth column represent the TP-average SCF bias for each season.

Figure 5 further shows the seasonal evolution of the SCF bias, as well as the snowfall and temperature biases. For the four reanalysis datasets, including ERA5, ERA5L, JRA55, and CFSR, snowfall (temperature) shows large positive (negative) biases during the accumulation

period, which together cause the large positive SCF bias during winter and spring. In contrast, both the snowfall and temperature biases are small during the ablation period, resulting in a small SCF bias. Thus, snowfall and temperature collectively explain the apparent seasonal variations in the SCF bias, as evidenced by the statistically significant correlations. Compared with snowfall, the temperature bias seems to have a greater impact, which is characterized by the larger R values. For MERRA2, CRAL, and GLDAS, the SCF biases remain small and stable across all four seasons, which corresponds to the well-simulated snowfall, despite the highly variable temperature bias. Therefore, snowfall may be more responsible for the seasonality in the SCF bias associated with these three reanalysis datasets.
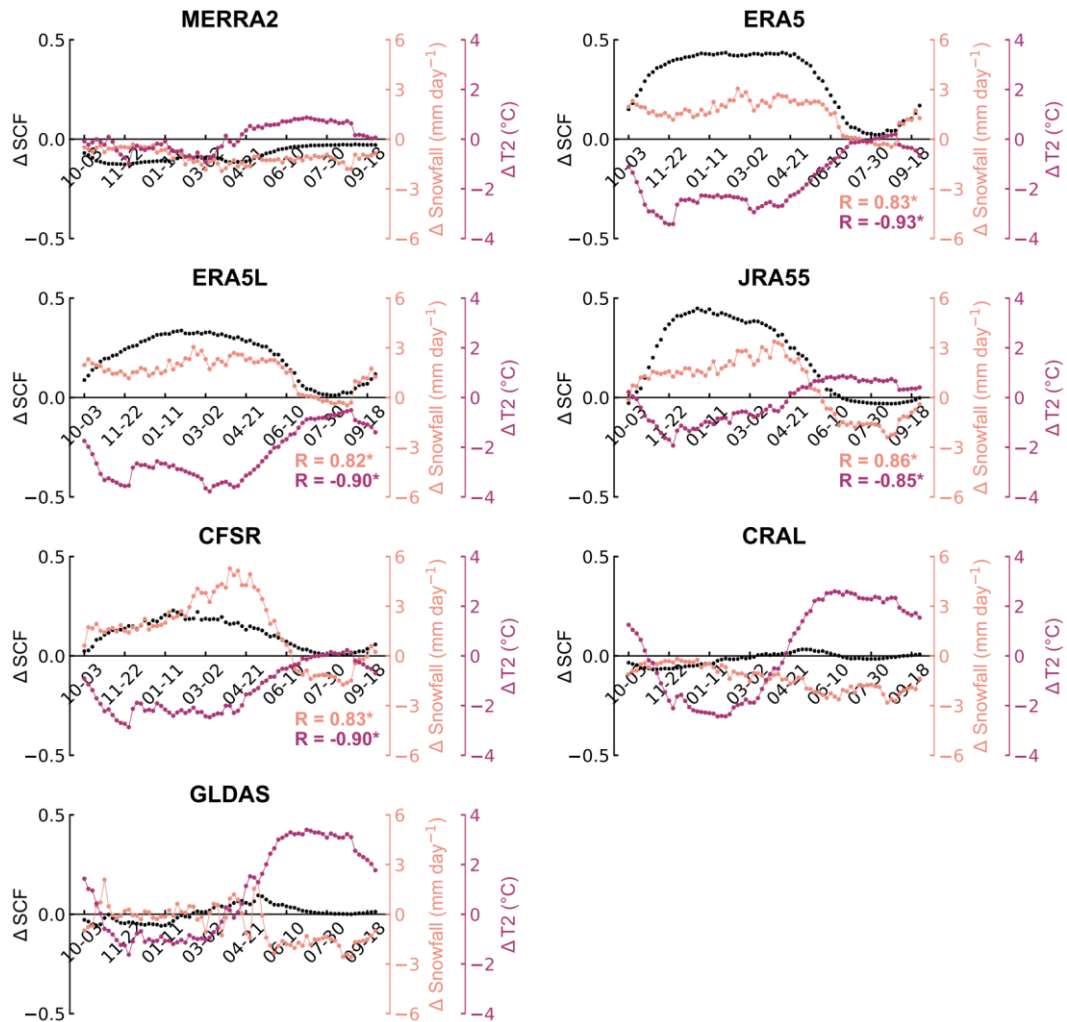
Figure 5: Temporal variations of SCF (black), snowfall (light pink), and temperature (purple) bias averaged at five-day intervals from all reanalysis datasets. R in light pink (purple) represents the correlation coefficient between snowfall (temperature) bias and SCF bias. The stars indicate the correlation exceeds the 95% confidence level. HMASR and MERRA2 share the same meteorological forcing data.

3.2.2 Evaluation of annual trends and bias attribution

505   Figure 6 presents the annual trends in SCF from WY 2001 to WY 2017 for the SPIReS and eight reanalysis datasets, as well as the CI values that characterize the agreement in SCF annual trends between the reanalysis datasets and SPIReS. The SPIReS generally show decreased SCF over the westerlies-dominated and east and southeast monsoon-dominated basins, but increased SCF over the east ITP, central Brahmaputra, and north Yangtze basins. However, these trends

510   are not statistically significant over most areas of the TP, indicating fluctuations in the variability of SCF over the past 17 years. This insignificant distribution over a wide area is also clearly demonstrated by snowfall trends in TPMFD (Fig. 7).

In comparison to SPIReS, ERA5L, ERA5, and JRA55 show greater variability in SCF annual trends, particularly noticeable in the Tarim basin and southeastern TP, where a

515   significant decrease in SCF is evident (Fig. 6a). Nevertheless, ERA5L, ERA5, and JRA55 still exhibit the most similar spatial patterns to SPIReS, with relatively high CI values for SCF trends in the TP, specifically 0.51, 0.48, and 0.49 respectively (Fig. 6b). This indicates their relatively well annual trends performance among the eight reanalysis datasets and can reproduce the SCF annual trend approximately half of the TP. This can be attributed to the superior spatial

520   consistency of ERA5L, ERA5, and JRA55 in simulating snowfall and temperature annual trends when compared with TPMFD (Fig. 7), as evidenced by CI values exceeding 0.5 for both snowfall and temperature annual trends (Table S3). For JRA55, suboptimal parameterization methods primarily affect the numerical magnitude of SCF simulation, resulting in higher RMSE and lower SS values in SCF climatological spatial distribution (see Section 3.1). However, the

525   parameterization process has minimal impact on the fluctuating variations of SCF over the time series, allowing JRA55 to demonstrate good annual trend performance (Fig. 6).
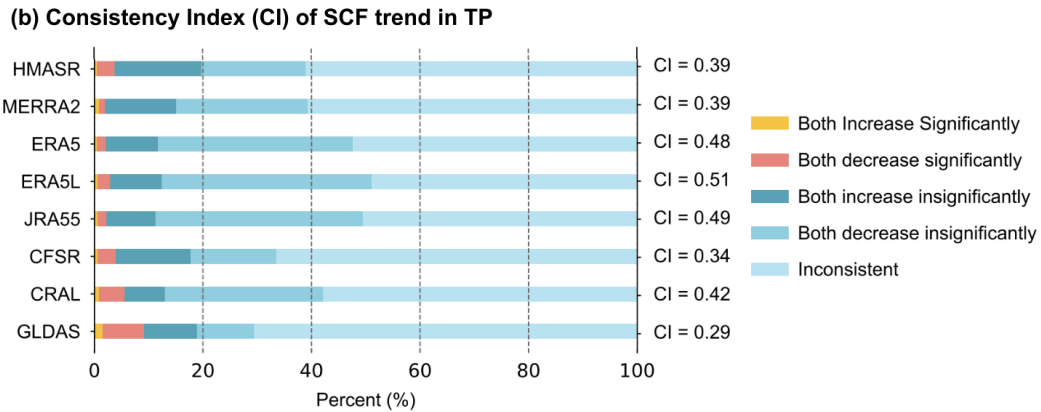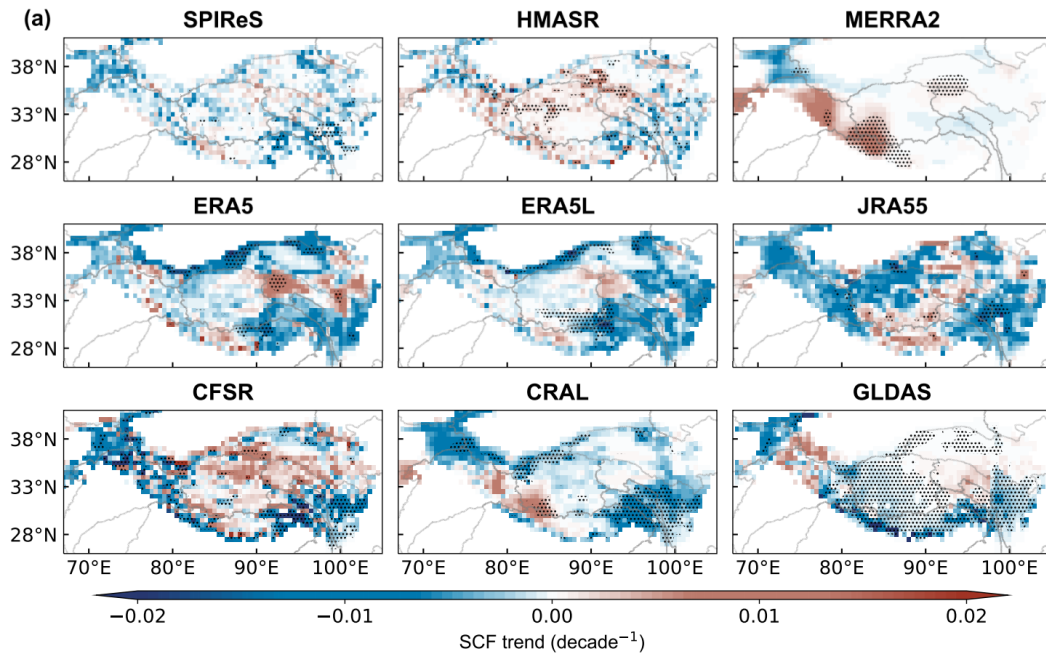
Figure 6: (a) Spatial distribution of the SCF annual trend from SPIReS and eight reanalysis datasets over the TP for the period WY 2001 to WY 2017. (b) The Consistency Index (CI) of SCF trends in reanalysis datasets with SPIReS over the TP.

The SCF annual trend of CRAL is statistically significant over approximately half of the TP, different from SPIReS. Consequently, CRAL demonstrates moderate performance in simulating SCF annual trends, similar to its spatial performance. CFSR presents highly uneven SCF annual trends with intermixed increases and decreases across pixel points, mirroring its snowfall and temperature annual trend distributions, resulting in poorer SCF annual trend performance with a CI value of only 0.34. GLDAS shows a significant decrease in SCF over more than 75% of the TP, markedly differing from SPIReS. While the widespread significant trends allow GLDAS to capture the most correct trends, reaching 9.25% (as indicated by the red and yellow bars in Fig. 6b), it also introduces a major drawback by misjudging too many insignificant SCF

540 fluctuations. Therefore, GLDAS has the lowest CI value of 0.29, with most basins having a CI value below 0.3 (Fig. S4). This is associated with its widespread and significant decreases in snowfall and increases in temperature annual trends (Fig. 7).
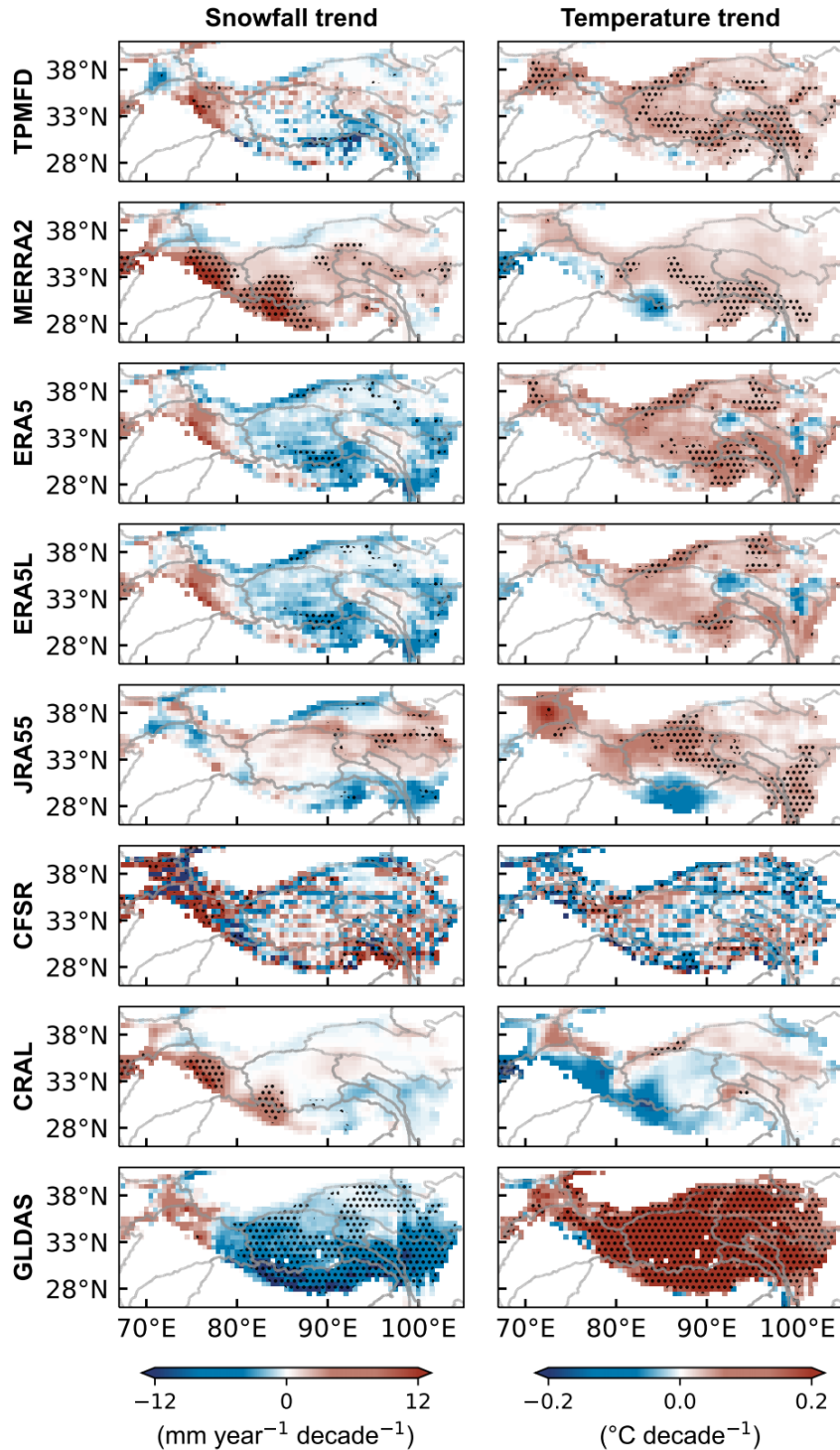
Figure 8: Spatial distribution of the snowfall annual trend from the reanalysis datasets over the TP for the period WY 2001 to WY 2017 (left), and the temperature annual trend (right). Black dots indicate that the trend exceeds the 95% confidence level. HMASR and MERRA2 share the same meteorological forcing data.

MERRA2 depicted a significantly increase trend in the southwestern TP, not align with SPIReS. This discrepancy is linked to MERRA2's erroneous portrayal of a significant increase in snowfall and a significant decrease in temperature in this region (Fig. 7). In contrast, HMASR, forced by the same meteorological input fields as MERRA2, partly corrected the falsely increase SCF trend in the southwestern TP and succeeded in capturing a significant declining trend in the southeastern TP, compared to MERRA2. This is evidenced by a higher proportion of correct significant trends (indicated by the red and yellow bars in Fig. 6b being greater for HMASR than for MERRA2). Moreover, the spatial pattern of HMASR SCF annual trends is more similar to SPIReS than MERRA2. However, when considering TP as a whole, the SCF trend simulations by HMASR showed limited improvement compared to MERRA2 as indicated by the similar CI values, yet still underperformed compared to ERA5L, ERA5, and JRA55. This suggests that data assimilation can only partially enhance SCF trend simulations, with meteorological forcings remaining the primary influencing factors.

4 Discussion

4.1 Influence of parameterization method on SCF

Figure 9 shows the SS and CI values of SCF simulations from each reanalysis dataset using the different parameterization methods. The parameterization process primarily affects the SCF value rather than the SCF phase variation over the time series, so our focus is on the spatial performance induced by the different parameterizations among the reanalysis datasets, indicated by the SS values obtained. For most reanalysis datasets, the MM_SCF method generates the best SCF simulation in terms of spatial performance with higher SS among most reanalysis datasets. This advantage is especially distinct for MERRA2 and ERA5. Moreover MM_SCF performs better than the built-in methods in ERA5, ERA5L, CRAL, and JRA55, demonstrating its broad applicability. The performance of ME_SCF is also good, with SS values slightly lower than those of MM_SCF. In contrast, MJ_SCF generally results in the poorest spatial performance across most reanalysis datasets, including JRA55, which uses MJ_SCF as

its built-in method. For the Noah_SCF methods, although they incorporate the complex impacts

575 of the underlying surface characteristics on SCF parameterization, the spatial performance of SCF is only comparable with that of MM_SCF and ME_SCF. This implies that considering the underlying surface characteristics has a limited impact on the accuracy of the SCF spatial simulations. We note that an appropriate parameterization method can actually improve SCF simulation. However, such improvements do not significantly alter the spatial performance

580 ranking of the eight reanalysis datasets; for instance, the SS values for MERRA2, ERA5, ERA5L, and JRA55 using the optimal MM_SCF method are still lower than those for HMASR using the poorest MJ_SCF method. This indirectly highlights the primary role of meteorological forcing inputs (snowfall and temperature) and snow assimilation with respect to SCF simulations. The influence of parameterization methods on the temporal performance of the

585 datasets, excluding CRAL, is limited, as indicated by small variations in the CI values among the reanalysis datasets.
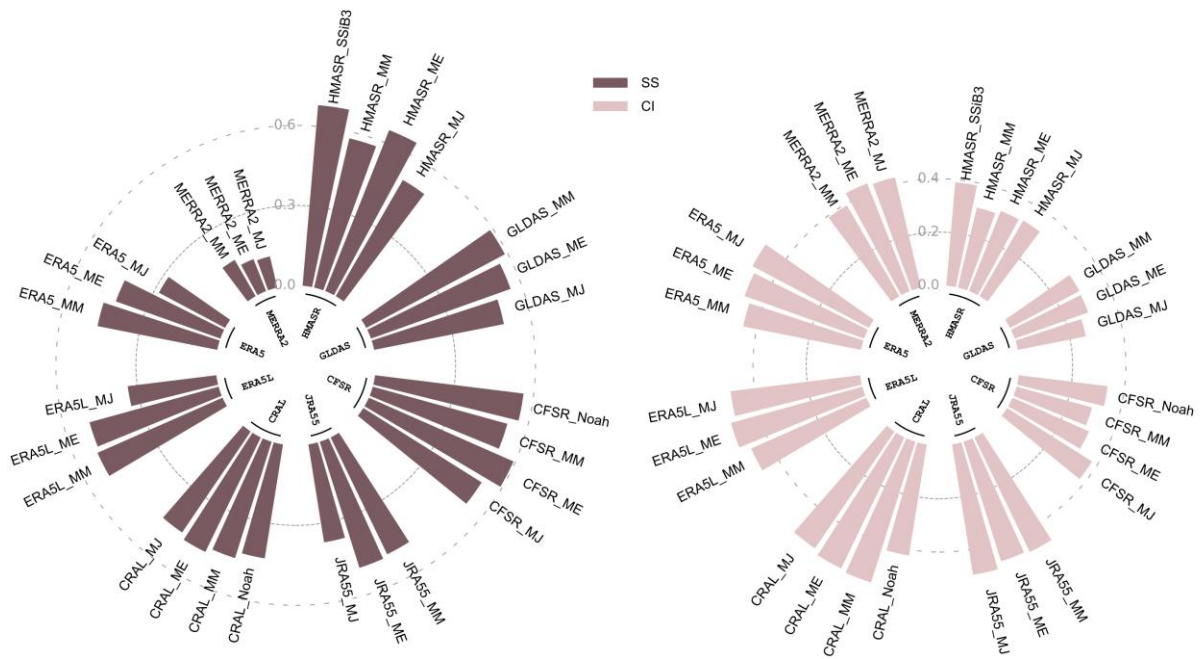
Figure 9: SS (left) and CI (right) values of SCF for all reanalysis datasets calculated offline using the MM_SCF, MJ_SCF, and ME_SCF parameterization methods.

590

4.2 Reanalysis dataset ensemble for SCF optimization

To optimize SCF simulation over the TP, we considered all possible combinations of the eight reanalysis datasets, identifying the best and worst combinations regarding both the spatial distribution and annual trend (Fig. 10). Our results reveal that the SCF accuracy does not monotonically improve with the number of combined datasets. For the spatial aspect, the SS value improves when transitioning from HMASR alone to a combination with GLDAS, but declines when more datasets are combined. The SS value with four datasets combined is lower than that achieved with HMASR alone, indicating that merging additional datasets does not always improve simulation accuracy, and may instead have a negative impact. Consequently, we concluded that a combination of HMASR and GLDAS is optimal for spatial SCF studies over the TP. This appears reasonable because HMASR and GLDAS have excellent accuracy in simulating the spatial variability of SCF, but the addition of poorly performing datasets (e.g., MERRA2 and JRA55) introduces more bias, resulting in a suboptimal outcome. From the trend aspect, the highest CI values are achieved by the combination of the three best-performing datasets for SCF annual trends, namely ERA5L, JRA55, and ERA5. Unlike SS, combining more datasets does not lead to a rapid decrease in CI values. The CI value from combining seven datasets still surpasses that obtained from ERA5L alone. Given the minor annual trend changes in SCF over the 17 years, all reanalysis datasets struggle to capture significant trend variations, displaying moderate annual trend performance. Thus, combining more datasets helps mitigate the shortcomings of individual datasets, enhancing overall trend accuracy. In contrast to the optimal combination, the worst combination shows a monotonically improving performance for both spatial distribution and annual trends. Notably, the worst combinations for SS and CI consistently include MERRA2 and GLDAS, whereas HMASR and ERA5L consistently contribute to the optimal combination for SS and CI. This corresponds with the results in Section 3.
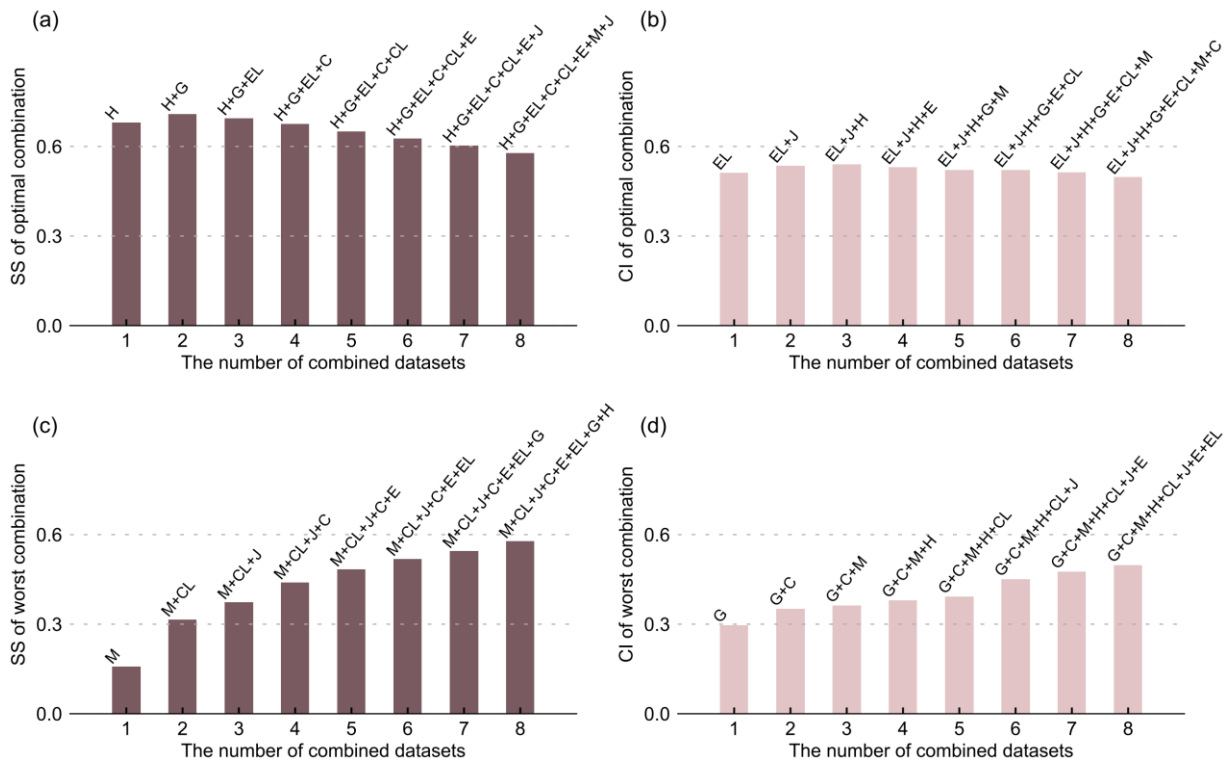
Figure 10: (a) SS for optimal reanalysis dataset combinations across varying numbers of datasets. (b) As in (a) but for CI. (c) and (d) As in (a) and (b), but for the worst combinations. H: HMASR; M: MERRA2; E: ERA5; EL: ERA5L; J: JRA55; C: CFSR; CL: CRAL; G: GLDAS.

4.3 Limitations

This study focused primarily on the impact of snowfall and temperature within snow models, as well as snow data assimilation and the choice of SCF parameterization, on the performance of reanalysis datasets in simulating SCF over the TP. However, other model parameters related to precipitation and temperature, such as the precipitation gradient used to describe precipitation variations at different elevations, and the critical temperature used to distinguish rain from snow, are equally vital to snow simulations (Zhang et al., 2015). Furthermore, snow, being a suspended substance, is susceptible to sublimation. It is estimated that blowing snow sublimation accounts for ~30% of global surface sublimation (Déry and Yau, 2002). The TP is perpetually influenced by the westerly jet stream, and processes such as blowing snow sublimation may be significant under windy and arid conditions. However, most LSMs used in reanalysis datasets do not consider blowing snow (Mortimer et al., 2020), and deficiencies in their model structures may also affect the accuracy of SCF simulations.

In addition to these factors, the spatial resolution of reanalysis datasets may also affect the accuracy of SCF simulations. Lei et al. (2023) pointed out that reanalysis datasets characterized by finer spatial resolutions exhibit better consistency with in situ measurements of SD over the TP; e.g., ERA5L outperforms ERA5 and MERRA2. In our study, the fine spatial resolution version of GLDAS generates better SCF simulations than the coarse spatial resolution version for both spatial distribution and annual trend (Fig. S1), which demonstrates the non-negligible impact of model resolution on the accuracy of SCF simulations. This also indirectly implies that the much finer resolution of $1/225° \times 1/225°$ may contribute to the outstanding performance of HMASR. However, SCF products with different spatial resolutions are available only in GLDAS. Therefore, this study cannot conclusively state that the impact of spatial resolution on SCF accuracy is universal.

5. Conclusions

Snow cover on the TP is sensitive to climate change. With global climate warming, the quantity and variability of SCF have become crucial indicators for understanding climate change and related hydrological processes. In this study, we assessed the ability and attributed the biases of eight widely used reanalysis datasets to simulate spatiotemporal variations in SCF over the TP based on SPIReS data covering the period WYs 2001–2017. The key findings are:

Among the eight reanalysis datasets, HMASR shows the least bias from SPIReS in simulating the spatial distribution of SCF climatology, achieving the highest R value of 0.87 and the highest SS value of 0.68. Additionally, it attains moderate accuracy in annual trend analysis. Overall, HMASR is the most suitable reanalysis dataset for SCF spatial simulation in the TP, benefiting from the direct assimilation of spectral unmixing algorithm derived SCF data from MODIS and Landsat satellites. GLDAS and CFSR are commendable for their spatial simulation accuracy of SCF, ranking just behind HMASR. However, their performance in annual trends is suboptimal, largely due to their poor representation of snowfall and temperature annual trends.

Conversely, ERA5 and ERA5L exhibit SCF overestimation across most of the TP, resulting in moderate SS values of 0.42 and 0.5 due to high RMSEs. Overestimated snowfall and underestimated temperature jointly contribute to the overestimation of SCF over most of the TP. Moreover, compared with snowfall, temperature-related physical processes have a more pronounced and widespread responsibility for SCF bias and the seasonal variation of SCF bias. Nevertheless, ERA5 and ERA5L show the best performance in annual trend simulations among the reanalysis datasets. The relatively good performance benefits from their accurate simulations of snowfall and temperature annual trends. JRA55, which overestimates SCF but performs well in annual trend, is more sensitive to the choice of SCF parameterization than to meteorological forcing factors. Moreover, its indirect assimilation of SD data does not effectively correct errors introduced by parameterization processing.

MERRA2, with the poorest spatial simulation indicated by the lowest STDR, R, and SS values, along with moderate CI values in annual trend simulation, ranks as the least effective reanalysis dataset for SCF simulation in the TP. This underperformance is attributed to errors in meteorological factors and a lack of snow data assimilation. CRAL demonstrates moderate accuracy in both spatial distribution and annual trend, which is consistent with its moderate performance in snowfall and temperature.

A two-member combined of HMASR and GLDAS is optimal for the study of SCF spatial scales, whereas a three-member combined of ERA5L, ERA5, and JRA55 is optimal for the study of annual trends.

These findings are crucial for selecting the most suitable reanalysis SCF datasets and gaining deeper insights into SCF variations and their controlling mechanisms on the TP. Reducing uncertainties within reanalysis SCF datasets stands as a pivotal stride toward refining climate models and prediction systems. Considering the significant impact of precipitation and temperature bias, along with snow assimilation, acquiring more precise meteorological forcing data and snow observation data is essential to further enhance the accuracy of reanalysis SCF simulations. Simultaneously, selecting more appropriate parameterization methods specific to reanalysis data models will contribute to improving dataset reliability. Optimizing simulations

of snow cover on the TP will provide critical support for future climate change research and response strategies.

Conflicts of interest

The authors declared that they have no conflicts of interest to this work. We declare that we do not have any commercial or associative interest that represents a conflict of interest in connection with the work submitted.

Data Availability Statement

The SPIReS product used in this work is publicly available from http://ftp.snow.ucsb.edu. The TPMFD dataset are obtained from the National Tibetan Plateau Science Data Center (TPDC; https://cstr.cn/18406.11.Atmos.tpdc.300398.). All the reanalysis data are publicly available and can be freely downloaded from the internet.

Acknowledgments

This research was supported by the National Science Fund for Distinguished Young Scholars (42025102), the Natural Science Foundation of Gansu province, China (21ZDKA0017), the National Natural Science Foundation of China (42375068, 42075061, and 42301142).

References

Adler, R.F., Huffman, G.J., Chang, A., Ferraro, R., Xie, P.-P., Janowiak, J., Rudolf, B., Schneider, U., Curtis, S.,

710   Bolvin, D., Gruber, A., Susskind, J., Arkin, P., Nelkin, E., 2003. The Version-2 Global Precipitation

Climatology Project (GPCP) monthly precipitation analysis (1979–present). J. Hydrometeorol. 4, 1147–1167.

https://doi.org/10.1175/1525-7541(2003)004<1147:TVGPCP>2.0.CO;2

Andreadis, K.M., Lettenmaier, D.P., 2006. Assimilating remotely sensed snow observations into a macroscale

hydrology model. Adv. Water Resour. 29, 872–886. https://doi.org/10.1016/j.advwatres.2005.08.004

715   Bair, E.H., Stillinger, T., Dozier, J., 2021. Snow Property Inversion from Remote Sensing (SPIReS): a generalized

multispectral unmixing approach with examples from MODIS and Landsat 8 OLI. IEEE Trans. Geosci.

Remote Sens. 59, 7270–7284. https://doi.org/10.1109/TGRS.2020.3040328

Bian, Q., Xu, Z., Zhao, L., Zhang, Y.-F., Zheng, H., Shi, C., Zhang, S., Xie, C., Yang, Z.-L., 2019. Evaluation and

intercomparison of multiple snow water equivalent products over the Tibetan Plateau. J. Hydrometeorol. 20,

720   2043–2055. https://doi.org/10.1175/JHM-D-19-0011.1

Brown, R.D., Brasnett, B., Robinson, D., 2003. Gridded North American monthly snow depth and snow water

equivalent for GCM evaluation. Atmosphere-Ocean 41, 1–14. https://doi.org/10.3137/ao.410101

Brown, R.D., Mote, P.W., 2009. The response of Northern Hemisphere snow cover to a changing climate*. J. Clim.

22, 2124–2145. https://doi.org/10.1175/2008JCLI2665.1

725   Cui, T., Li, C., Tian, F., 2021. Evaluation of Temperature and Precipitation Simulations in CMIP6 Models Over

the Tibetan Plateau. Earth Space Sci. 8, e2020EA001620. https://doi.org/10.1029/2020EA001620

Danielson, J.J., Gesch, D.B., 2011. Global multi-resolution terrain elevation data 2010 (GMTED2010) (No. 2011–

1073), Open-File Report. U.S. Geological Survey. https://doi.org/10.3133/ofr20111073

de Rosnay, P., Balsamo, G., Albergel, C., Muñoz-Sabater, J., Isaksen, L., 2014. Initialisation of land surface

730   variables for numerical weather prediction. Surv. Geophys. 35, 607–621. https://doi.org/10.1007/s10712-012-

9207-x

Deng, H., Pepin, N.C., Chen, Y., 2017. Changes of snowfall under warming in the Tibetan Plateau. J. Geophys.

Res. Atmospheres 122, 7323–7341. https://doi.org/10.1002/2017JD026524

Déry, S.J., Yau, M.K., 2002. Large-scale mass balance effects of blowing snow and surface sublimation. J. Geophys.

735   Res. Atmospheres 107, ACL 8-1-ACL 8-17. https://doi.org/10.1029/2001JD001251

Ding, B., Yang, K., Qin, J., Wang, L., Chen, Y., He, X., 2014. The dependence of precipitation types on surface elevation and meteorological conditions and its parameterization. J. Hydrol. 513, 154–163. https://doi.org/10.1016/j.jhydrol.2014.03.038

Dozier, J., Painter, T.H., Rittger, K., Frew, J.E., 2008. Time–space continuity of daily maps of fractional snow cover and albedo from MODIS. Adv. Water Resour. 31, 1515–1526. https://doi.org/10.1016/j.advwatres.2008.08.011

Dutra, E., Kotlarski, S., Viterbo, P., Balsamo, G., Miranda, P.M.A., Schär, C., Bissolli, P., Jonas, T., 2011. Snow cover sensitivity to horizontal resolution, parameterizations, and atmospheric forcing in a land surface model. J. Geophys. Res. Atmospheres 116. https://doi.org/10.1029/2011JD016061

ECMWF, 2018. IFS Documentation CY45R1-Part IV : Physical processes, in: IFS Documentation CY45R1, IFS Documentation. ECMWF. https://doi.org/10.21957/4whwo8jw0

Ek, M.B., Mitchell, K.E., Lin, Y., Rogers, E., Grunmann, P., Koren, V., Gayno, G., Tarpley, J.D., 2003. Implementation of Noah land surface model advances in the National Centers for Environmental Prediction operational mesoscale Eta model. J. Geophys. Res. Atmospheres 108, 2002JD003296. https://doi.org/10.1029/2002JD003296

Fujiwara, M., Wright, J.S., Manney, G.L., Gray, L.J., Anstey, J., Birner, T., Davis, S., Gerber, E.P., Harvey, V.L., Hegglin, M.I., Homeyer, C.R., Knox, J.A., Krüger, K., Lambert, A., Long, C.S., Martineau, P., Molod, A., Monge-Sanz, B.M., Santee, M.L., Tegtmeier, S., Chabrillat, S., Tan, D.G.H., Jackson, D.R., Polavarapu, S., Compo, G.P., Dragani, R., Ebisuzaki, W., Harada, Y., Kobayashi, C., McCarty, W., Onogi, K., Pawson, S., Simmons, A., Wargan, K., Whitaker, J.S., Zou, C.-Z., 2017. Introduction to the SPARC Reanalysis Intercomparison Project (S-RIP) and overview of the reanalysis systems. Atmos. Chem. Phys. 17, 1417–1452. https://doi.org/10.5194/acp-17-1417-2017

Gelaro, R., McCarty, W., Suárez, M.J., Todling, R., Molod, A., Takacs, L., Randles, C.A., Darmenov, A., Bosilovich, M.G., Reichle, R., Wargan, K., Coy, L., Cullather, R., Draper, C., Akella, S., Buchard, V., Conaty, A., Silva, A.M. da, Gu, W., Kim, G.-K., Koster, R., Lucchesi, R., Merkova, D., Nielsen, J.E., Partyka, G., Pawson, S., Putman, W., Rienecker, M., Schubert, S.D., Sienkiewicz, M., Zhao, B., 2017. The Modern-Era Retrospective analysis for Research and Applications, version 2 (MERRA-2). J. Clim. 30, 5419–5454. https://doi.org/10.1175/JCLI-D-16-0758.1

Hall, D.K., Riggs, G.A., Salomonson, V.V., DiGirolamo, N.E., Bayr, K.J., 2002. MODIS snow-cover products. Remote Sens. Environ. 83, 181–194. https://doi.org/10.1016/S0034-4257(02)00095-0

Helfrich, S.R., McNamara, D., Ramsay, B.H., Baldwin, T., Kasheta, T., 2007. Enhancements to, and forthcoming developments in the Interactive Multisensor Snow and Ice Mapping System (IMS). Hydrol. Process. 21, 1576–1586. https://doi.org/10.1002/hyp.6720

Hernández-Henríquez, M.A., Déry, S.J., Derksen, C., 2015. Polar amplification and elevation-dependence in trends of Northern Hemisphere snow cover extent, 1971–2014. Environ. Res. Lett. 10, 044010. https://doi.org/10.1088/1748-9326/10/4/044010

Hersbach, H., Bell, B., Berrisford, P., Hirahara, S., Horányi, A., Muñoz-Sabater, J., Nicolas, J., Peubey, C., Radu, R., Schepers, D., Simmons, A., Soci, C., Abdalla, S., Abellan, X., Balsamo, G., Bechtold, P., Biavati, G., Bidlot, J., Bonavita, M., Chiara, G., Dahlgren, P., Dee, D., Diamantakis, M., Dragani, R., Flemming, J., Forbes, R., Fuentes, M., Geer, A., Haimberger, L., Healy, S., Hogan, R.J., Hólm, E., Janisková, M., Keeley, S., Laloyaux, P., Lopez, P., Lupu, C., Radnoti, G., Rosnay, P., Rozum, I., Vamborg, F., Villaume, S., Thépaut, J., 2020. The ERA5 global reanalysis. Q. J. R. Meteorol. Soc. 146, 1999–2049. https://doi.org/10.1002/qj.3803

Huang, J., Zhou, X., Wu, G., Xu, X., Zhao, Q., Liu, Yimin, Duan, A., Xie, Y., Ma, Y., Zhao, P., Yang, S., Yang, K., Yang, H., Bian, J., Fu, Y., Ge, J., Liu, Yuzhi, Wu, Q., Yu, H., Wang, B., Bao, Q., Qie, K., 2023. Global climate impacts of land - surface and atmospheric processes over the Tibetan Plateau. Rev. Geophys. 61, e2022RG000771. https://doi.org/10.1029/2022RG000771

Huffman, G.J., Adler, R.F., Morrissey, M.M., Bolvin, D.T., Curtis, S., Joyce, R., McGavock, B., Susskind, J., 2001. Global precipitation at one-degree daily resolution from multisatellite observations. J. Hydrometeorol. 2, 36–50. https://doi.org/10.1175/1525-7541(2001)002<0036:GPAODD>2.0.CO;2

Immerzeel, W.W., Van Beek, L.P.H., Bierkens, M.F.P., 2010. Climate change will affect the Asian water towers. Science 328, 1382–1385. https://doi.org/10.1126/science.1183188

Jiang, Y., Chen, F., Gao, Y., He, C., Barlage, M., Huang, W., 2020. Assessment of uncertainty sources in snow cover simulation in the Tibetan Plateau. J. Geophys. Res. Atmospheres 125. https://doi.org/10.1029/2020JD032674

Jiang, Y., Yang, K., Qi, Y., Zhou, X., He, J., Lu, H., Li, Xin, Chen, Y., Li, Xiaodong, Zhou, B., Mamtimin, A., Shao, C., Ma, X., Tian, J., Zhou, J., 2023. TPHiPr: a long-term (1979–2020) high-accuracy precipitation dataset (1

／30°, daily) for the Third Pole region based on high-resolution atmospheric modeling and dense observations. Earth Syst. Sci. Data 15, 621–638. https://doi.org/10.5194/essd-15-621-2023

Kendall, M.G., 1975. Rank Correlation Methods. J. Inst. Actuar. 75, 140–141. https://doi.org/10.1017/S0020268100013019

Kitoh, A., Arakawa, O., 2016. Reduction in the east–west contrast in water budget over the Tibetan Plateau under a future climate. Hydrol. Res. Lett. 10, 113–118. https://doi.org/10.3178/hrl.10.113

Kobayashi, S., Ota, Y., Harada, Y., Ebita, A., Moriya, M., Onoda, H., Onogi, K., Kamahori, H., Kobayashi, C., Endo, H., Miyaoka, K., Takahashi, K., 2015. The JRA-55 Reanalysis: General Specifications and Basic Characteristics. J. Meteorol. Soc. Jpn. Ser II 93, 5–48. https://doi.org/10.2151/jmsj.2015-001

Koster, R.D., Suarez, M.J., Ducharne, A., Stieglitz, M., Kumar, P., 2000. A catchment-based approach to modeling land surface processes in a general circulation model: 1. Model structure. J. Geophys. Res. Atmospheres 105, 24809–24822. https://doi.org/10.1029/2000JD900327

Lehner, B., Verdin, K., Jarvis, A., 2008. New Global Hydrography Derived From Spaceborne Elevation Data. Eos Trans. Am. Geophys. Union 89, 93–94. https://doi.org/10.1029/2008EO100001

Lei, Y., Pan, J., Xiong, C., Jiang, L., Shi, J., 2023. Snow depth and snow cover over the Tibetan Plateau observed from space in against ERA5: matters of scale. Clim. Dyn. 60, 1523–1541. https://doi.org/10.1007/s00382-022-06376-0

Li, Q., Yang, T., Li, L., 2022. Evaluation of snow depth and snow cover represented by multiple datasets over the Tianshan Mountains: Remote sensing, reanalysis, and simulation. Int. J. Climatol. 42, 4223–4239. https://doi.org/10.1002/joc.7459

Liang, X., Jiang, L., Pan, Y., Shi, C., Liu, Z., Zhou, Z., 2020. A 10-Yr global land surface reanalysis interim dataset (CRA-Interim/Land): Implementation and preliminary evaluation. J. Meteorol. Res. 34, 101–116. https://doi.org/10.1007/s13351-020-9083-0

Lin, H., Wu, Z., 2011. Contribution of the autumn Tibetan Plateau snow cover to seasonal prediction of North American winter temperature. J. Clim. 24, 2801–2813. https://doi.org/10.1175/2010JCLI3889.1

Liu, Y., Fang, Y., Li, D., Margulis, S.A., 2022. How well do global snow products characterize snow storage in High Mountain Asia? Geophys. Res. Lett. 49. https://doi.org/10.1029/2022GL100082

Liu, Y., Fang, Y., Margulis, S.A., 2021. Spatiotemporal distribution of seasonal snow water equivalent in High

820   Mountain Asia from an 18-year Landsat–MODIS era snow reanalysis dataset. The Cryosphere 15, 5261–5280. https://doi.org/10.5194/tc-15-5261-2021

Liu, Z., Jiang, L., Shi, C., Zhang, T., Zhou, Z., Liao, J., Yao, S., Liu, J., Wang, M., Wang, H., Liang, X., Zhang, Z., Yao, Y., Zhu, T., Chen, Z., Xu, W., Cao, L., Jiang, H., Hu, K., 2023. CRA-40/Atmosphere—the first-generation Chinese atmospheric reanalysis (1979–2018): System description and performance evaluation. J.

825   Meteorol. Res. 37, 1–19. https://doi.org/10.1007/s13351-023-2086-x

Luo, J., Chen, H., Zhou, B., 2020. Comparison of Snowfall Variations over China Identified from Different Snowfall/Rainfall Discrimination Methods. J. Meteorol. Res. 34, 1114–1128. https://doi.org/10.1007/s13351-020-0004-z

Lyu, M., Wen, M., Wu, Z., 2018. Possible contribution of the inter-annual Tibetan Plateau snow cover variation to

830   the Madden-Julian oscillation convection variability. Int. J. Climatol. 38, 3787–3800. https://doi.org/10.1002/joc.5533

Magnusson, J., Winstral, A., Stordal, A.S., Essery, R., Jonas, T., 2017. Improving physically based snow simulations by assimilating snow depths using the particle filter. Water Resour. Res. 53, 1125–1143. https://doi.org/10.1002/2016WR019092

835   Ma, Y., Ma, W., Zhong, L., Hu, Z., Li, M., Zhu, Z., Han, C., Wang, B., Liu, X., 2017. Monitoring and Modeling the Tibetan Plateau's climate system and its impact on East Asia. Sci. Rep. 7, 44574. https://doi.org/10.1038/srep44574

Ma, Y., Wang, B., Chen, X., Zhong, L., Hu, Z., Ma, W., Han, C., Li, M., 2022. Strengthening the three-dimensional comprehensive observation system of multi-layer interaction on the Tibetan Plateau to cope with the warming

840   and wetting trend. Atmospheric Ocean. Sci. Lett. 15, 100224. https://doi.org/10.1016/j.aosl.2022.100224

Magnusson, J., Winstral, A., Stordal, A.S., Essery, R., Jonas, T., 2017. Improving physically based snow simulations by assimilating snow depths using the particle filter. Water Resour. Res. 53, 1125–1143. https://doi.org/10.1002/2016WR019092

Mann, H.B., 1945. Nonparametric tests against trend. Econometrica 13, 245–259. https://doi.org/10.2307/1907187

845   Meng, J., Yang, R., Wei, H., Ek, M., Gayno, G., Xie, P., Mitchell, K., 2012. The land surface analysis in the NCEP climate forecast system reanalysis. J. Hydrometeorol. 13, 1621–1630. https://doi.org/10.1175/JHM-D-11-090.1

Mortimer, C., Mudryk, L., Derksen, C., Luojus, K., Brown, R., Kelly, R., Tedesco, M., 2020. Evaluation of long-term Northern Hemisphere snow water equivalent products. The Cryosphere 14, 1579–1594. https://doi.org/10.5194/tc-14-1579-2020

Mudryk, L.R., Derksen, C., Kushner, P.J., Brown, R., 2015. Characterization of Northern Hemisphere snow water equivalent datasets, 1981–2010. J. Clim. 28, 8037–8051. https://doi.org/10.1175/JCLI-D-15-0229.1

Muñoz-Sabater, J., Dutra, E., Agustí-Panareda, A., Albergel, C., Arduini, G., Balsamo, G., Boussetta, S., Choulga, M., Harrigan, S., Hersbach, H., Martens, B., Miralles, D.G., Piles, M., Rodríguez-Fernández, N.J., Zsoter, E., Buontempo, C., Thépaut, J.-N., 2021. ERA5-Land: a state-of-the-art global reanalysis dataset for land applications. Earth Syst. Sci. Data 13, 4349–4383. https://doi.org/10.5194/essd-13-4349-2021

Onogi, K., Tsutsui, J., Koide, H., Sakamoto, M., Kobayashi, S., Hatsushika, H., Matsumoto, T., Yamazaki, N., Kamahori, H., Takahashi, K., Kadokura, S., Wada, K., Kato, K., Oyama, R., Ose, T., Mannoji, N., Taira, R., 2007. The JRA-25 reanalysis. J. Meteorol. Soc. Jpn. 85, 369–432. https://doi.org/10.2151/jmsj.85.369

Orsolini, Y., Wegmann, M., Dutra, E., Liu, B., Balsamo, G., Yang, K., De Rosnay, P., Zhu, C., Wang, W., Senan, R., Arduini, G., 2019. Evaluation of snow depth and snow cover over the Tibetan Plateau in global reanalysis using in situ and satellite remote sensing observations. The Cryosphere 13, 2221–2239. https://doi.org/10.5194/tc-13-2221-2019

Painter, T.H., Rittger, K., McKenzie, C., Slaughter, P., Davis, R.E., Dozier, J., 2009. Retrieval of subpixel snow covered area, grain size, and albedo from MODIS. Remote Sens. Environ. 113, 868–879. https://doi.org/10.1016/j.rse.2009.01.001

Qiu, J., 2008. China: The third pole. Nature 454, 393–396. https://doi.org/10.1038/454393a

Reichle, R.H., Draper, C.S., Liu, Q., Girotto, M., Mahanama, S.P.P., Koster, R.D., Lannoy, G.J.M.D., 2017. Assessment of MERRA-2 Land Surface Hydrology Estimates. J. Clim. 30, 2937–2960. https://doi.org/10.1175/JCLI-D-16-0720.1

Rodell, M., Houser, P.R., Jambor, U., Gottschalck, J., Mitchell, K., Meng, C.-J., Arsenault, K., Cosgrove, B., Radakovich, J., Bosilovich, M., Entin, J.K., Walker, J.P., Lohmann, D., Toll, D., 2004. The global land data assimilation system. Bull. Am. Meteorol. Soc. 85, 381–394. https://doi.org/10.1175/BAMS-85-3-381

Saha, S., Moorthi, S., Pan, H.-L., Wu, X., Wang, Jiande, Nadiga, S., Tripp, P., Kistler, R., Woollen, J., Behringer, D., Liu, H., Stokes, D., Grumbine, R., Gayno, G., Wang, Jun, Hou, Y.-T., Chuang, H., Juang, H.-M.H., Sela,

J., Iredell, M., Treadon, R., Kleist, D., Van Delst, P., Keyser, D., Derber, J., Ek, M., Meng, J., Wei, H., Yang, R., Lord, S., Van Den Dool, H., Kumar, A., Wang, W., Long, C., Chelliah, M., Xue, Y., Huang, B., Schemm, J.-K., Ebisuzaki, W., Lin, R., Xie, P., Chen, M., Zhou, S., Higgins, W., Zou, C.-Z., Liu, Q., Chen, Y., Han, Y., Cucurull, L., Reynolds, R.W., Rutledge, G., Goldberg, M., 2010. The NCEP climate forecast system reanalysis. Bull. Am. Meteorol. Soc. 91, 1015–1058. https://doi.org/10.1175/2010BAMS3001.1

Saha, S., Moorthi, S., Wu, X., Wang, J., Nadiga, S., Tripp, P., Behringer, D., Hou, Y.-T., Chuang, H., Iredell, M., Ek, M., Meng, J., Yang, R., Mendez, M.P., Van Den Dool, H., Zhang, Q., Wang, W., Chen, M., Becker, E., 2014. The NCEP climate forecast system version 2. J. Clim. 27, 2185–2208. https://doi.org/10.1175/JCLI-D-12-00823.1

Sato, N., Sellers, P.J., Randall, D.A., Schneider, E.K., Shukla, J., Kinter, J.L., Hou, Y.-T., Albertazzi, E., 1989. Effects of implementing the Simple Biosphere Model in a general circulation model. J. Atmospheric Sci. 46, 2757–2782. https://doi.org/10.1175/1520-0469(1989)046<2757:EOITSB>2.0.CO;2

Sellers, P.J., Mintz, Y., Sud, Y.C., Dalcher, A., 1986. A Simple Biosphere Model (SIB) for use within general circulation models. J. Atmospheric Sci. 43, 505–531. https://doi.org/10.1175/1520-0469(1986)043<0505:ASBMFU>2.0.CO;2

Serquet, G., Marty, C., Dulex, J.-P., Rebetez, M., 2011. Seasonal trends and temperature dependence of the snowfall/precipitation-day ratio in Switzerland. Geophys. Res. Lett. 38. https://doi.org/10.1029/2011GL046976

Sheffield, J., Goteti, G., Wood, E.F., 2006. Development of a 50-Year High-Resolution Global Dataset of Meteorological Forcings for Land Surface Modeling. J. Clim. 19, 3088–3111. https://doi.org/10.1175/JCLI3790.1

Stillinger, T., Rittger, K., Raleigh, M.S., Michell, A., Davis, R.E., Bair, E.H., 2023. Landsat, MODIS, and VIIRS snow cover mapping algorithm performance as validated by airborne lidar datasets. The Cryosphere 17, 567–590. https://doi.org/10.5194/tc-17-567-2023

Sun, C., Walker, J.P., Houser, P.R., 2004. A methodology for snow data assimilation in a land surface model. J. Geophys. Res. Atmospheres 109, 2003JD003765. https://doi.org/10.1029/2003JD003765

Sun, S., Xue, Y., 2001. Implementing a new snow scheme in Simplified Simple Biosphere Model. Adv. Atmospheric Sci. 18, 335–354. https://doi.org/10.1007/BF02919314

Taylor, K.E., 2001. Summarizing multiple aspects of model performance in a single diagram. J. Geophys. Res. Atmospheres 106, 7183–7192. https://doi.org/10.1029/2000JD900719

Thackeray, C.W., Fletcher, C.G., Mudryk, L.R., Derksen, C., 2016. Quantifying the Uncertainty in Historical and Future Simulations of Northern Hemisphere Spring Snow Cover. J. Clim. 29, 8647–8663. https://doi.org/10.1175/JCLI-D-16-0341.1

Vorkauf, M., Marty, C., Kahmen, A., Hiltbrunner, E., 2021. Past and future snowmelt trends in the Swiss Alps: the role of temperature and snowpack. Clim. Change 165, 44. https://doi.org/10.1007/s10584-021-03027-x

Wang, A., Zeng, X., 2012. Evaluation of multireanalysis products with in situ observations over the Tibetan Plateau. J. Geophys. Res. Atmospheres 117, D05102. https://doi.org/10.1029/2011JD016553

Wegmann, M., Orsolini, Y., Dutra, E., Bulygina, O., Sterin, A., Brönnimann, S., 2017. Eurasian snow depth in long-term climate reanalyses. The Cryosphere 11, 923–935. https://doi.org/10.5194/tc-11-923-2017

Xie, P., Arkin, P.A., 1997. Global precipitation: A 17-year monthly analysis based on gauge observations, satellite estimates, and numerical model Outputs. Bull. Am. Meteorol. Soc. 78, 2539–2558. https://doi.org/10.1175/1520-0477(1997)078<2539:GPAYMA>2.0.CO;2

Xie, P., Chen, M., Yang, S., Yatagai, A., Hayasaka, T., Fukushima, Y., Liu, C., 2007. A gauge-based analysis of daily precipitation over East Asia. J. Hydrometeorol. 8, 607–626. https://doi.org/10.1175/JHM583.1

Xu, W., Ma, L., Ma, M., Zhang, H., Yuan, W., 2017. Spatial–temporal variability of snow cover and depth in the Qinghai–Tibetan Plateau. J. Clim. 30, 1521–1533. https://doi.org/10.1175/JCLI-D-15-0732.1

Xu, X., Lu, C., Shi, X., Gao, S., 2008. World water tower: An atmospheric perspective. Geophys. Res. Lett. 35, L20815. https://doi.org/10.1029/2008GL035867

Xue, Y., Sun, S., Kahan, D.S., Jiao, Y., 2003. Impact of parameterizations in snow physics and interface processes on the simulation of snow cover and runoff at several cold region sites. J. Geophys. Res. Atmospheres 108, 2002JD003174. https://doi.org/10.1029/2002JD003174

Yang, D., Ding, M., Dou, T., Han, W., Liu, W., Zhang, J., Du, Z., Xiao, C., 2021. On the Differences in Precipitation Type Between the Arctic, Antarctica and Tibetan Plateau. Front. Earth Sci. 9. https://doi.org/10.3389/feart.2021.607487

Yang, K., Jiang, Z., Tang, W., He, J., Shao, C., Zhou, X., Lu, H., Chen, Y., Li, X., Shi, J., 2023. A high-resolution near-surface meteorological forcing dataset for the Third Pole region (TPMFD, 1979-2022). Natl. Tibet.

Plateau Data Cent. https://doi.org/10.11888/Atmos.tpdc.300398

Yang, M., Wang, X., Pang, G., Wan, G., Liu, Z., 2019. The Tibetan Plateau cryosphere: Observations and model simulations for current status and recent changes. Earth-Sci. Rev. 190, 353–369. https://doi.org/10.1016/j.earscirev.2018.12.018

Yao, T., Thompson, L., Yang, W., Yu, W., Gao, Y., Guo, X., Yang, X., Duan, K., Zhao, H., Xu, B., Pu, J., Lu, A., Xiang, Y., Kattel, D.B., Joswiak, D., 2012. Different glacier status with atmospheric circulations in Tibetan Plateau and surroundings. Nat. Clim. Change 2, 663–667. https://doi.org/10.1038/nclimate1580

Yao, T., Xue, Y., Chen, D., Chen, Fahu, Thompson, L., Cui, P., Koike, T., Lau, W.K.-M., Lettenmaier, D., Mosbrugger, V., Zhang, R., Xu, B., Dozier, J., Gillespie, T., Gu, Y., Kang, S., Piao, S., Sugimoto, S., Ueno, K., Wang, L., Wang, W., Zhang, F., Sheng, Y., Guo, W., Ailikun, Yang, X., Ma, Y., Shen, S.S.P., Su, Z., Chen, Fei, Liang, S., Liu, Y., Singh, V.P., Yang, K., Yang, D., Zhao, X., Qian, Y., Zhang, Y., Li, Q., 2019. Recent Third Pole's Rapid Warming Accompanies Cryospheric Melt and Water Cycle Intensification and Interactions between Monsoon and Environment: Multidisciplinary Approach with Observations, Modeling, and Analysis. Bull. Am. Meteorol. Soc. 100, 423–444. https://doi.org/10.1175/BAMS-D-17-0057.1

You, Q., Wu, F., Wang, H., Jiang, Z., Pepin, N., Kang, S., 2020a. Projected changes in snow water equivalent over the Tibetan Plateau under global warming of 1.5° and 2°C. J. Clim. 33, 5141–5154. https://doi.org/10.1175/JCLI-D-19-0719.1

You, Q., Wu, T., Shen, L., Pepin, N., Zhang, L., Jiang, Z., Wu, Z., Kang, S., AghaKouchak, A., 2020b. Review of snow cover variation over the Tibetan Plateau and its influence on the broad climate system. Earth-Sci. Rev. 201, 103043. https://doi.org/10.1016/j.earscirev.2019.103043

Yu, L., Zhang, S., Bu, K., Yang, J., Yan, F., Chang, L., 2013. A review on snow data sets. Sci. Geogr. Sin. 33, 878–883. https://doi.org/10.13249/j.cnki.sgs.2013.07.878

Zhang, F., Zhang, H., Hagen, S.C., Ye, M., Wang, D., Gui, D., Zeng, C., Tian, L., Liu, J., 2015. Snow cover and runoff modelling in a high mountain catchment with scarce data: effects of temperature and precipitation parameters. Hydrol. Process. 29, 52–65. https://doi.org/10.1002/hyp.10125

Zhang, H., Immerzeel, W.W., Zhang, F., De Kok, R.J., Chen, D., Yan, W., 2022. Snow cover persistence reverses the altitudinal patterns of warming above and below 5000 m on the Tibetan Plateau. Sci. Total Environ. 803, 149889. https://doi.org/10.1016/j.scitotenv.2021.149889

Zhang, H., Zhang, F., Che, T., Yan, W., Ye, M., 2021. Investigating the ability of multiple reanalysis datasets to simulate snow depth variability over mainland China from 1981 to 2018. J. Clim. 34, 9957–9972. https://doi.org/10.1175/JCLI-D-20-0804.1

Zhang, T., 2005. Influence of the seasonal snow cover on the ground thermal regime: An overview. Rev. Geophys. 43, RG4002. https://doi.org/10.1029/2004RG000157

Zhou, X., Yang, K., Ouyang, L., Wang, Y., Jiang, Y., Li, X., Chen, D., Prein, A., 2021. Added value of kilometer-scale modeling over the third pole region: a CORDEX-CPTP pilot study. Clim. Dyn. 57, 1673–1687. https://doi.org/10.1007/s00382-021-05653-8

Zhu, X., Wu, T., Li, R., Wang, S., Hu, G., Wang, W., Qin, Y., Yang, S., 2017. Characteristics of the ratios of snow, rain and sleet to precipitation on the Qinghai-Tibet Plateau during 1961–2014. Quat. Int., Third Pole: The Last 20,000 Years - Part 2 444, 137–150. https://doi.org/10.1016/j.quaint.2016.07.030